ELEC3027 Radio Communications
Background Information on Amplitude Modulation

1 Analogue Modulation

1.1 Amplitude Modulation

When a Radio Frequency (RF) signal is placed onto the antenna of a transmitter, it will propagate through free space and can be detected on the antenna of a receiver. The higher the frequency of this signal, the smaller the antennas that are required. However, we are often interested in communicating relatively low frequency message signals, such as audio. Hence, we must modulate our low frequency message signal onto a high frequency *carrier*, in order to transmit it. This has the added benefit of allowing us to modulate different message signals onto different carrier frequencies, in order to transmit them without interfering with each other.

Figure 1 shows the schematic of a transmission scheme that uses Amplitude Modulation (AM) to transmit a time-varying input signal $x(t)$, as well as demodulation to obtain a received signal $\hat{x}(t)$.

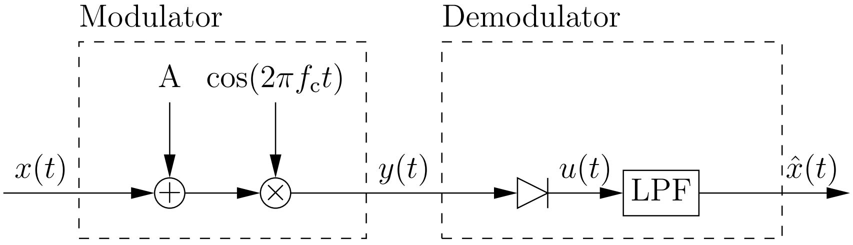

Figure 1: AM modulation and demodulation.

1.1.1 Operation

The AM modulator of Figure 1 uses the message signal $x(t)$ to vary the amplitude of the carrier sinusoid $\cos(2\pi f_c t)$, where the carrier frequency f_c is usually much higher than the highest frequency in the message signal. As shown in Figure 1

$$y(t) = [A + x(t)] \cos(2\pi f_c t), \tag{1}$$

where A is a constant DC offset.

In the AM demodulator of Figure 1, the diode symbol represents a *rectifier* which gives

$$u(t) = \begin{cases} y(t) & \text{if } y(t) > 0 \\ 0 & \text{otherwise} \end{cases} . \tag{2}$$

Finally, the *Low Pass Filter* (LPF) of Figure 1 is employed to provide the reconstructed message signal $\hat{x}(t)$. In order to show how the demodulator works, let's consider some examples in the next sections.

1.1.2 Example 1

Suppose that the message signal of Figure 1 is a simple sinewave $x(t) = \cos(2\pi f_{\mathrm{m}} t)$ having a frequency of $f_{\mathrm{m}} = 20$ kHz, as shown in Figure 2. Note that in addition to the *time domain* plot of $x(t)$, Figure 2 uses the *Power Spectral Density* (PSD) of $x(t)$ to show it in the *frequency domain.*

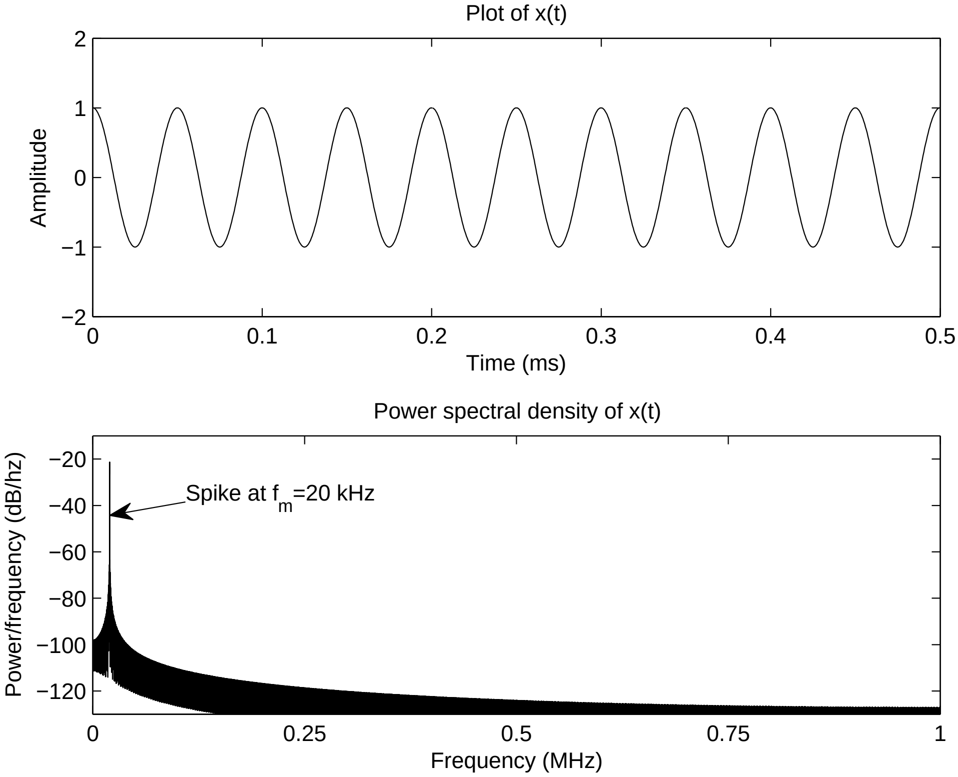

Figure 2: Plot and PSD for the message signal $x(t) = \cos(2\pi f_{\mathrm{m}} t)$, where $f_{\mathrm{m}} = 20$ kHz.

Put simply, *Fourier theory* states that any message signal $x(t)$ can be constructed from a sum of sinusoids, having different frequencies and various amplitudes (as well as phases). Essentially, the PSD of Figure 2 shows the frequencies of those sinusoids that have high amplitudes. Since our message signal $x(t) = \cos(2\pi f_{\mathrm{m}} t)$ can be thought of as a sum of just a single $f_{\mathrm{m}} = 20$ kHz sinusoid, the PSD of Figure 2 contains only a single spike at this frequency, showing that it is the only frequency that is associated with a high amplitude in $x(t)$.

Using the signal $x(t) = \cos(2\pi f_{\rm m} t)$, Equation 1 becomes

$$y(t) = [A + \cos(2\pi f_{\rm m} t)] \cos(2\pi f_{\rm c} t). \tag{3}$$

Using the trigonometric identity $\cos(\alpha)\cos(\beta) = \frac{1}{2}\cos(\alpha - \beta) + \frac{1}{2}\cos(\alpha + \beta)$, we obtain

$$y(t) = A\cos(2\pi f_{\rm c} t) + \frac{1}{2}\cos(2\pi[f_{\rm c} - f_{\rm m}]t) + \frac{1}{2}\cos(2\pi[f_{\rm c} + f_{\rm m}]t). \tag{4}$$

This shows that when $x(t) = \cos(2\pi f_{\rm m} t)$, the AM signal $y(t)$ is the sum of three sinusoids:

- one with a frequency equal to the difference between the carrier and message frequencies $[f_{\rm c} - f_{\rm m}]$;
- one with a frequency equal to the carrier frequency $f_{\rm c}$;
- one with a frequency equal to the sum of the carrier and message frequencies $[f_{\rm c} + f_{\rm m}]$.

Figure 3 provides the plot and PSD of the resultant modulated signal $y(t)$ for the case where a carrier frequency of $f_{\rm c} = 250$ kHz and a DC offset of $A = 1.5$ are used. Note that the signal $x(t)$ acts as an *envelope* for the carrier sinusoid. Also note that in accordance with Fourier theory, the PSD of $y(t)$ contains spikes at the three frequencies listed above, namely $[f_{\rm c} - f_{\rm m}] = 230$ kHz, $f_{\rm c} = 250$ kHz and $[f_{\rm c} + f_{\rm m}] = 270$ kHz. In other words, each spike corresponds to a different term in Equation 4, as identified by the annotations in Figure 3.

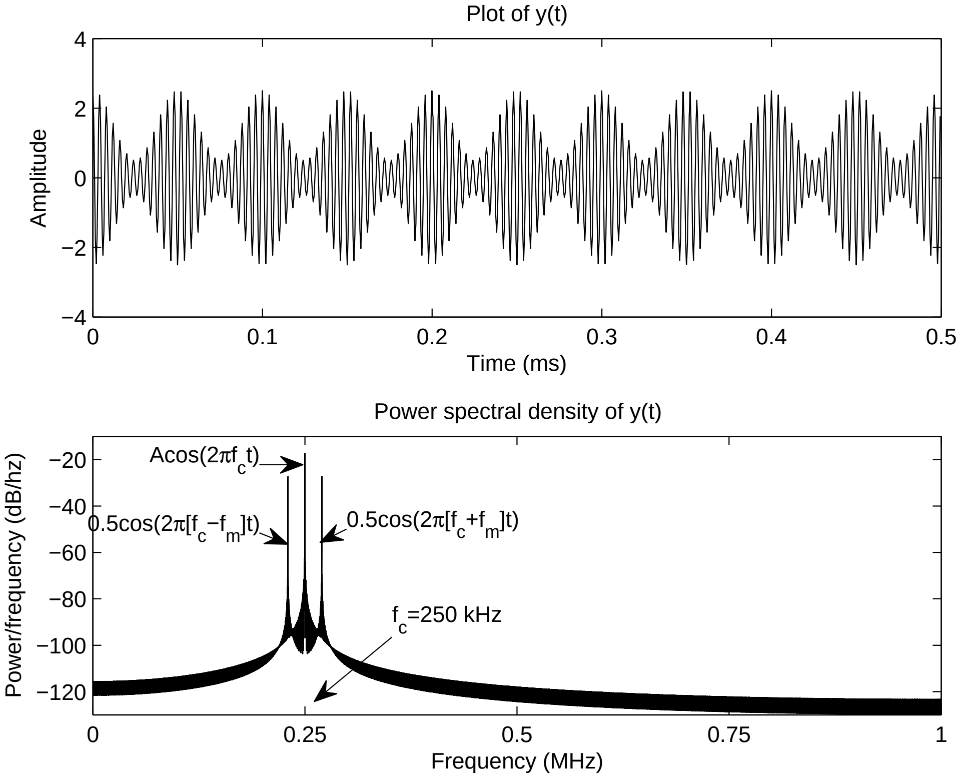

Figure 3: Plot and PSD for the modulated signal $y(t)$, for the case where the message signal $x(t)$ of Figure 2 is modulated onto a carrier having a frequency of $f_{\rm c} = 250$ kHz, using a DC offset of $A = 1.5$, as shown in Figure 1.

Figure 4 shows the corresponding signals that are obtained by the demodulator of Figure 1. In accordance with Equation 2, the rectifier of Figure 1 clips the negative part of the modulated signal $y(t)$ in order to provide $u(t)$. Following this, the reconstructed message signal $\hat{x}(t)$ is obtained by simply smoothing away the high frequency oscillations in the signal $u(t)$. This is achieved by the LPF of Figure 1, which only passes the low frequency part of $u(t)$ that corresponds to the message signal $x(t)$. As shown in Figure 4, the resultant reconstructed message signal $\hat{x}(t)$ is the same as the message signal $x(t)$ of Figure 2 (apart from a DC offset and a scaling factor, which are easily remedied).

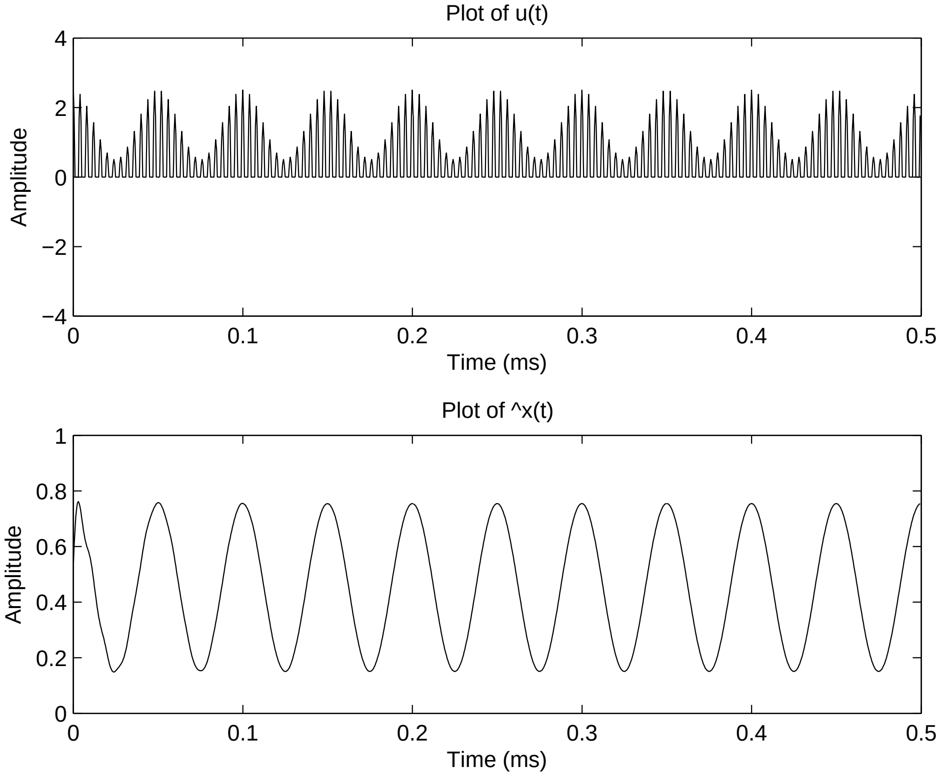

Figure 4: Plots of the signals $u(t)$ and $\hat{x}(t)$, for the case where the modulated signal $y(t)$ of Figure 3 is demodulated as shown in Figure 1.

1.1.3 Example 2

Let's now consider the case where the more intricate message signal $x(t)$ of Figure 5 is transmitted using the AM scheme of Figure 1. This message signal can be thought of as comprising a sum of many sinusoids, which have frequencies no greater than $f_{\text{max}} = 10$ kHz, as shown in the Power Spectral Density (PSD) plot of Figure 5.

Figure 3 provides the plot and PSD of the resultant modulated signal $y(t)$ for the case where a carrier frequency of $f_{\text{c}} = 250$ kHz and a DC offset of $A = 1.5$ are used to modulate the message signal $x(t)$ of Figure 5. Again, the message signal $x(t)$ can be seen to act as an envelope for the carrier sinusoid.

As Equation 4 implies, for each of the many sinusoids that comprise the message signal $x(t)$, a pair of sinusoids is generated in $y(t)$, having frequencies on either side of the carrier frequency f_{c}. The group of sinusoids having frequencies above the carrier frequency f_{c} are referred to as

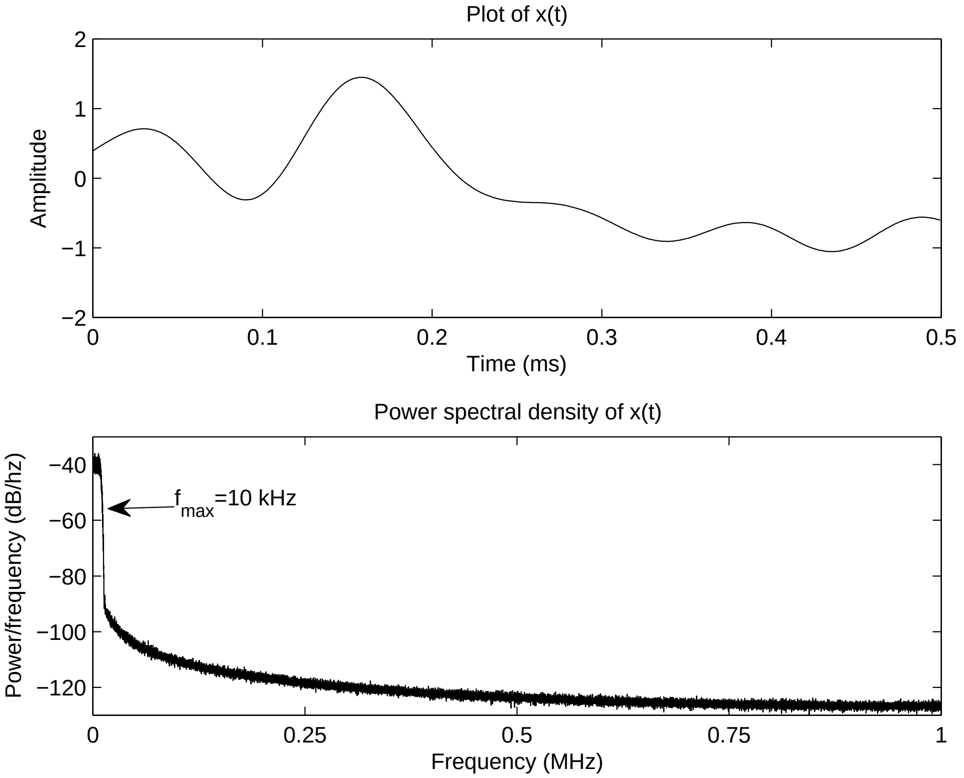

Figure 5: Example plot and PSD for the message signal $x(t)$ of Figure 1.

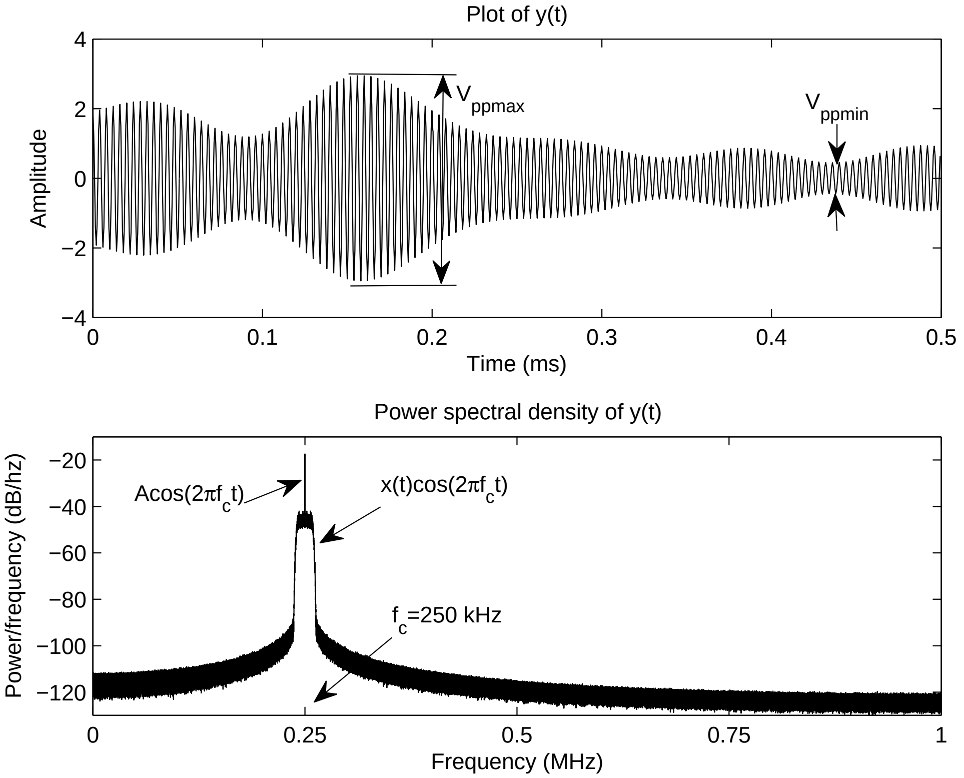

Figure 6: Plot and PSD for the modulated signal $y(t)$, for the case where the message signal $x(t)$ of Figure 5 is modulated onto a carrier having a frequency of $f_c = 250$ kHz, using a DC offset of $A = 1.5$, as shown in Figure 1.

the *upper sideband*. Similarly, the group having frequencies below f_c are the *lower sideband*. It is these sidebands that contain all of the message information. Note that the sinusoid at the carrier frequency f_c does not contain any message information. However, it is still useful since it helps the receiver to 'lock-on' to the transmission.

As in the first example, the demodulator of Figure 1 is able to reconstruct the message signal $x(t)$, as shown in Figure 7.

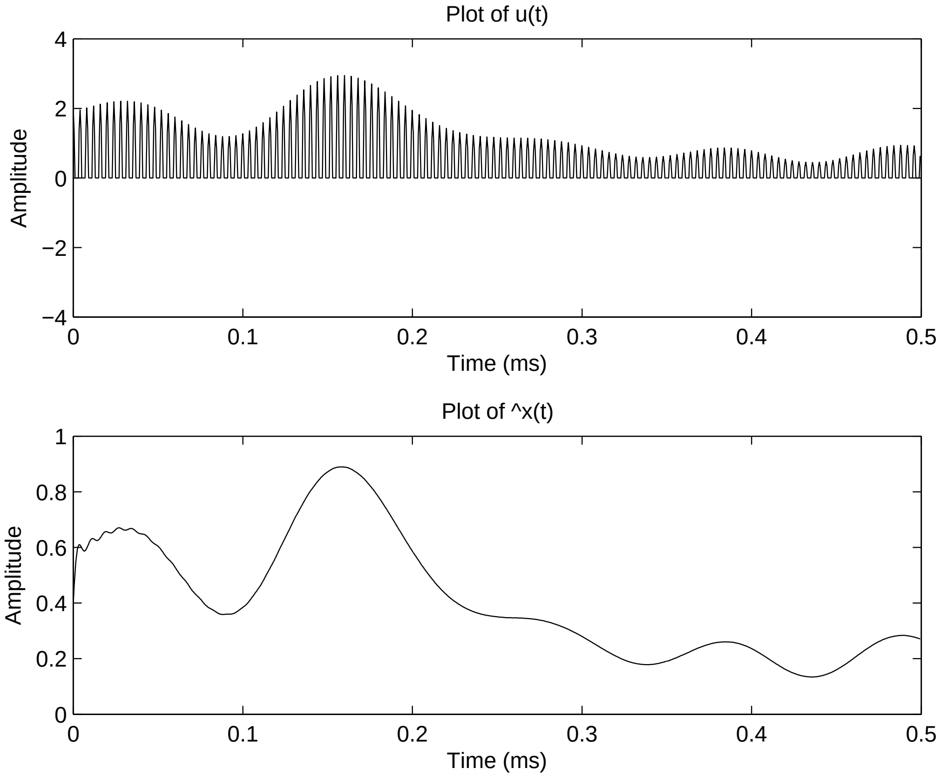

Figure 7: Plots of the signals $u(t)$ and $\hat{x}(t)$, for the case where the modulated signal $y(t)$ of Figure 6 is demodulated as shown in Figure 1.

Observe in Figure 5 that the maximum and minimum amplitudes of the signal $x(t)$ are $\max[x(t)] \approx 1.5$ and $\min[x(t)] \approx -1$. As shown in Figure 6, these values affect the maximum and minimum *peak-to-peak* amplitudes of the modulated signal $y(t)$. Provided that the DC offset satisfies $A > -\min[x(t)]$, the peak-to-peak amplitudes are given by

$$V_{\text{ppmax}} = 2(A + \max[x(t)]), \tag{5}$$

$$V_{\text{ppmin}} = 2(A + \min[x(t)]). \tag{6}$$

In the example of Figure 6, we obtain $V_{\text{ppmax}} = 6$ and $V_{\text{ppmin}} = 1$, since it employs a DC offset of $A = 1.5$.

The *modulation factor* m of a modulated signal $y(t)$ is defined as

$$m = \frac{V_{\text{ppmax}} - V_{\text{ppmin}}}{V_{\text{ppmax}} + V_{\text{ppmin}}}. \tag{7}$$

Note that in cases where the DC offset A is large, V_{ppmax} and V_{ppmin} will have similar values and the modulation factor will be close to zero. As A is reduced towards $-\min[x(t)]$, V_{ppmin} will approach zero and the modulation factor m will increase towards one. Since the modulation factor is in the range $[0, 1]$, it can be expressed as a percentage, whereupon it is called the *modulation index.* When the modulation index is less than 100%, the AM signal $y(t)$ is said to be *undermodulated.* By contrast, the AM signal $y(t)$ is said to be *100% modulated* when the modulation index is 100%.

Note that if the DC offset does not satisfy $A > -\min[x(t)]$, then the AM signal $y(t)$ becomes *overmodulated.* In this case, the demodulator of Figure 1 is unable to reconstruct the message signal $x(t)$ because the envelope of the modulated signal will cross-over itself, as shown for $A = 0.5$ in Figure 8. The result is that the parts of $x(t)$ that do not satisfy $A > -x(t)$ become inverted in the reconstructed message signal $\hat{x}(t)$, as shown in Figure 8.

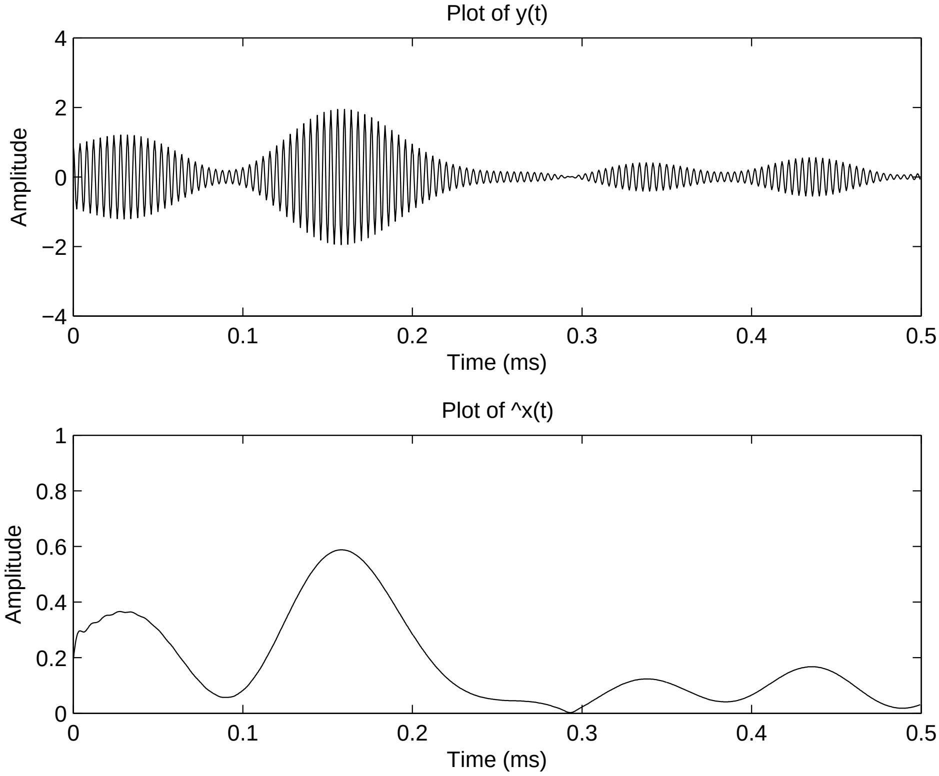

Figure 8: Plots of the signals $y(t)$ and $\hat{x}(t)$, for the case where the message signal $x(t)$ of Figure 5 is overmodulated using a DC offset of $A = 0.5$ as shown in Figure 1.

1.2 Double SideBand Suppressed Carrier Modulation

In Section 1.1 we considered AM, which adds a DC offset A to the message signal $x(t)$ in order to facilitate a simple demodulator, comprising only a rectifier and an LPF. In addition to its simplicity, the demodulator of Section 1.1 has the advantage of being *non-coherent*, which means that it does not require knowledge of the carrier frequency and phase in order to perform demodulation. However, the AM scheme of Section 1.1 fails when the DC offset is not large enough to prevent overmodulation, as described in Section 1.1.3.

In this section we consider a modulation scheme that can successfully perform demodulation when the DC offset is not large enough to prevent overmodulation. In fact, the modulation scheme considered in this section does not require a DC offset at all, as shown in the schematic of Figure 9. Since removing the DC offset is equivalent to setting $A = 0$, Equation 4 implies that the sinusoid at the carrier frequency f_c is removed or *suppressed* from the modulated signal $y(t)$, leaving only the two sidebands. For this reason, the modulation scheme considered in this section is called *Double SideBand Suppressed Carrier* (DSBSC) modulation.

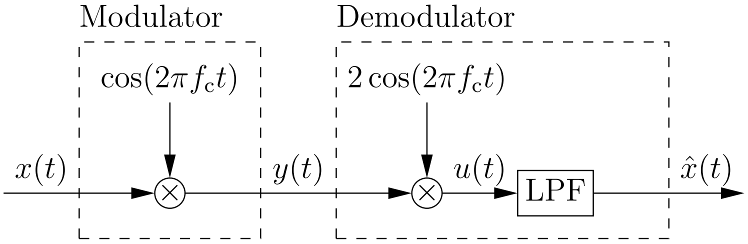

Figure 9: DSBSC modulation and demodulation.

The advantage of omitting the sinusoid at the carrier frequency is that this makes DSBSC much more power efficient than AM. This is because the sinusoid at the carrier frequency typically accounts for a large fraction of the transmit power in AM, but does not carry any information about the message signal $x(t)$. However, the disadvantage is that *coherent* demodulation is required. More specifically, the demodulator is required to use carrier recovery techniques in order to determine the exact frequency and phase of the carrier sinusoid. These are required in order to generate the signal $2\cos(2\pi f_c t)$ that is used to perform demodulation in Figure 9. In Section 1.5, we will see what happens if the wrong frequency or phase are used for this signal.

1.2.1 Mathematics

In order to understand the operation of the DSBSC scheme shown in Figure 9, let's consider the associated mathematics. As shown in Figure 9

$$y(t) = x(t)\cos(2\pi f_c t), \tag{8}$$

$$u(t) = 2x(t)\cos(2\pi f_c t)\cos(2\pi f_c t). \tag{9}$$

Using the trigonometric identity $2\cos(\theta)\cos(\theta) = 1 + \cos(2\theta)$, we get

$$u(t) = x(t)\left(1 + \cos(4\pi f_c t)\right), \tag{10}$$

$$= x(t) + x(t)\cos(4\pi f_c t). \tag{11}$$

The signal $u(t)$ contains a high frequency component $x(t)\cos(4\pi f_c t)$, which is filtered away by the LPF of Figure 9. As a result, the signal $x(t)$ is reconstructed

$$\hat{x}(t) = x(t). \tag{12}$$

1.2.2 Example

Suppose that the message signal $x(t)$ of Figure 5 is modulated onto an $f_c = 250$ kHz carrier, as shown in Figure 9. The resultant signal $y(t) = x(t)\cos(2\pi f_c t)$ is obtained by using $x(t)$ to *envelope* the carrier wave $\cos(2\pi f_c t)$, as shown in Figure 10. The PSD of $y(t)$ is obtained by *convolving* the *double-sided PSD* of $x(t)$ with the PSD of the carrier wave, which resembles an impulse at $f_c = 250$ kHz. This convolution moves the double-sided PSD to the location of the impulse, as shown in Figure 10.

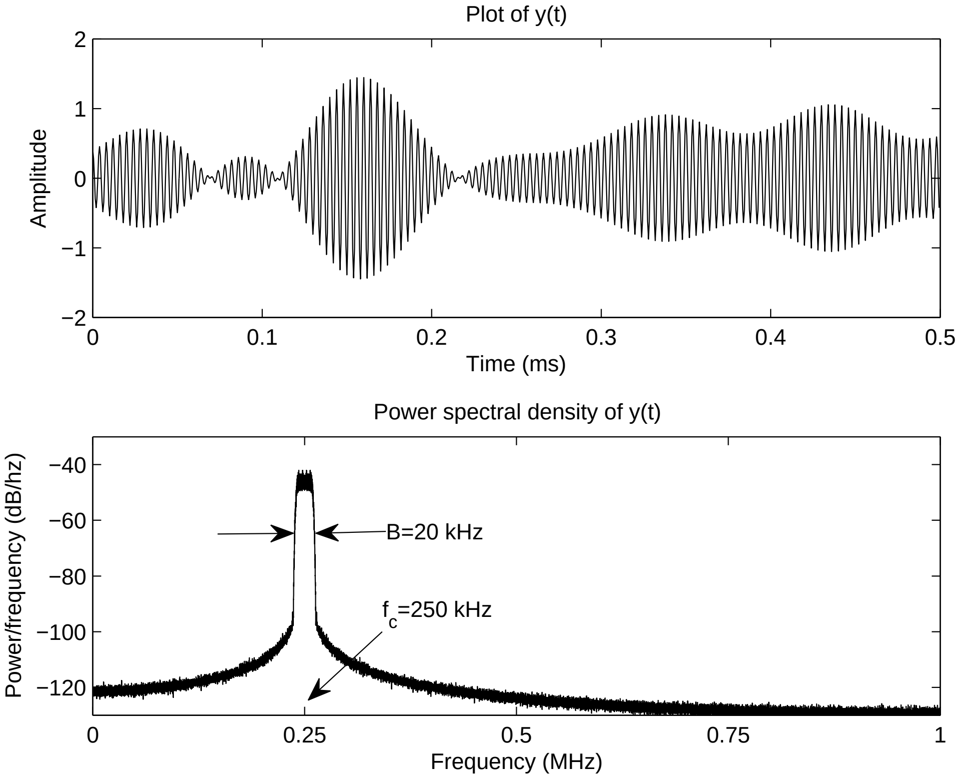

Figure 10: Example plot and PSD for the modulated signal $y(t)$ of Figure 9.

Here, the double-sided PSD of $x(t)$ can be obtained by mirroring the single-sided PSD shown in Figure 10 about a frequency of 0 Hz (and subtracting 3 dB from all non-zero frequencies). This mirroring introduces negative frequencies. It may seem strange to use negative frequencies, but they're convenient because they make the described convolution work. The strangeness surrounding negative frequencies can be mitigated by considering that $\cos(\theta) = \cos(-\theta)$. Hence, $\cos(2\pi ft) = 0.5\cos(2\pi ft) + 0.5\cos(2\pi(-f)t)$. Therefore, any component of a signal can be thought of as having half its power at a positive frequency and the other half at the corresponding negative frequency. Note that halving the power is achieved by subtracting the 3 dB that is mentioned in brackets above.

As shown in Figure 10, the bandwidth of the signal $y(t)$ is $B = 20$ kHz, where

$$B = 2f_{\max}. \tag{13}$$

In the receiver of Figure 9, the signal $u(t) = x(t) + x(t)\cos(4\pi f_c t)$ appears as shown in Figure 11. As shown in the PSD of Figure 11, the component $x(t)\cos(4\pi f_c t)$ may be removed by the LPF of Figure 9, which requires a cutoff frequency of between 10 and 490 kHz.

1.3 Quadrature Amplitude Modulation

So far, we have only considered the use of a cosine carrier wave. If we had used a sine carrier wave in Section 1.2, we would have obtained very similar results. This is because the sine and cosine functions differ only by a phase shift of $\pi/2$ radians, ie $\cos(\theta) = \sin(\theta + \pi/2)$. As a result, $\sin(\theta) = 0$ if $\cos(\theta) = \pm 1$ and $\cos(\theta) = 0$ if $\sin(\theta) = \pm 1$. These results indicate that

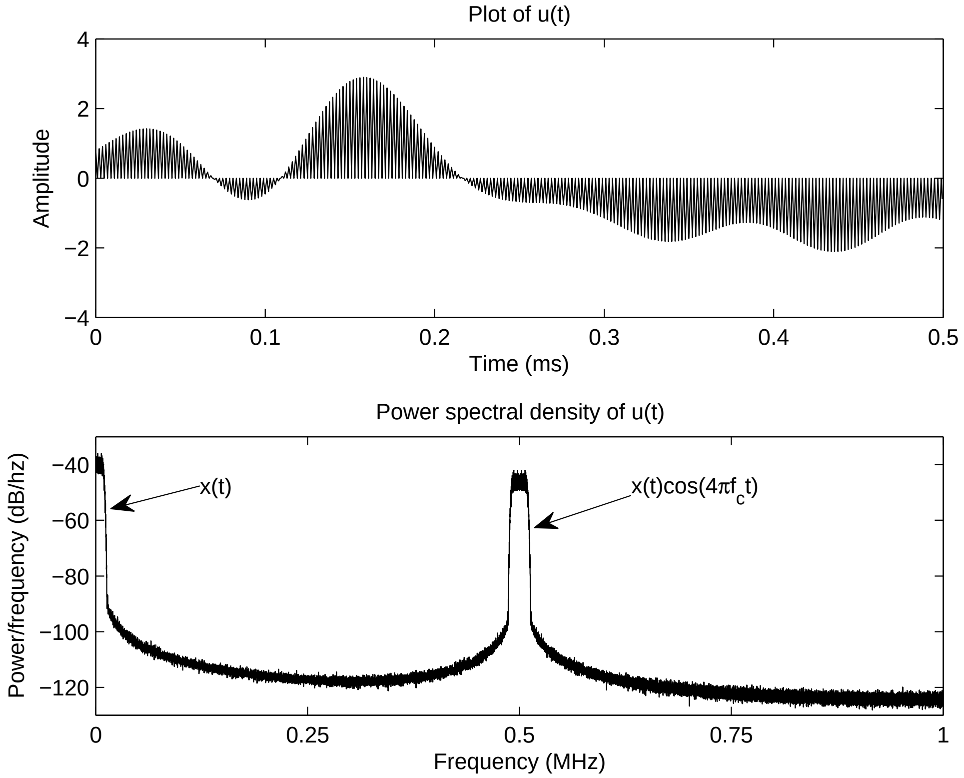

Figure 11: Example plot and PSD for the modulated signal $u(t)$ of Figure 9.

the cosine and sine functions are *orthogonal* to each other. This means that a signal $x_{\mathrm{i}}(t)$ that is amplitude modulated onto a cosine carrier wave will not interfere with another signal $x_{\mathrm{q}}(t)$ that is modulated onto a sine carrier wave having the same frequency f_{c}. In this way, we can transmit two signals at once, which is useful for stereo audio for example. We refer to these signals as the *in-phase signal* $x_{\mathrm{i}}(t)$ and the *quadrature-phase signal* $x_{\mathrm{q}}(t)$. The additional presence of the quadrature-phase signal gives *Quadrature Amplitude Modulation* (QAM) its name. A schematic for a QAM scheme is shown in Figure 12.

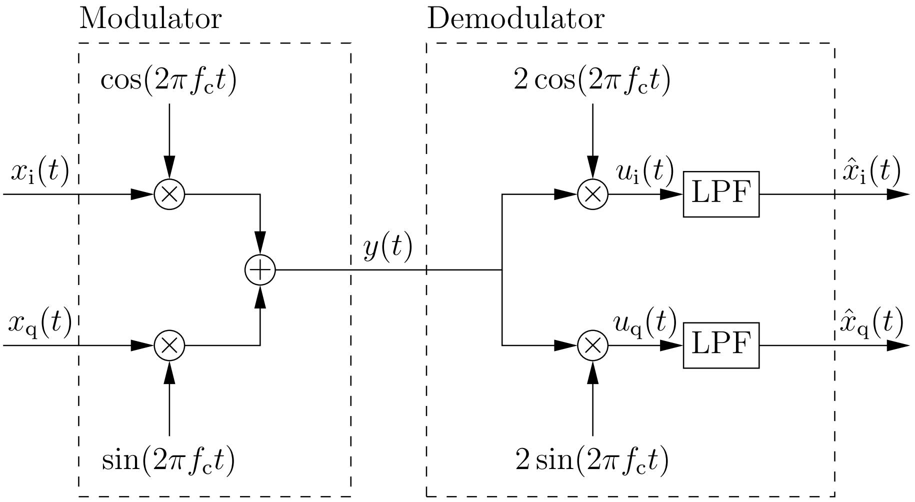

Figure 12: QAM modulation and demodulation.

As shown in Figure 12

$$y(t) = x_{\mathrm{i}}(t)\cos(2\pi f_{\mathrm{c}}t) + x_{\mathrm{q}}(t)\sin(2\pi f_{\mathrm{c}}t), \tag{14}$$

$$u_{\mathrm{i}}(t) = 2x_{\mathrm{i}}(t)\cos(2\pi f_{\mathrm{c}}t)\cos(2\pi f_{\mathrm{c}}t) + 2x_{\mathrm{q}}(t)\sin(2\pi f_{\mathrm{c}}t)\cos(2\pi f_{\mathrm{c}}t), \tag{15}$$

$$u_{\mathrm{q}}(t) = 2x_{\mathrm{q}}(t)\sin(2\pi f_{\mathrm{c}}t)\sin(2\pi f_{\mathrm{c}}t) + 2x_{\mathrm{i}}(t)\cos(2\pi f_{\mathrm{c}}t)\sin(2\pi f_{\mathrm{c}}t). \tag{16}$$

Note that as in the DSBSC scheme shown in Figure 9, the QAM modulated signal $y(t)$ of Figure 12 has a bandwidth of $B = 2f_{\max}$. The QAM scheme can therefore transmit double the amount of information in the same amount of bandwidth. It pays for this by requiring double the amount of transmit power, double the amount of hardware and a more sophisticated mechanism for synchronising the receiver with the transmitter.

Using the trigonometric identities $2\cos(\theta)\cos(\theta) = 1 + \cos(2\theta)$, $2\sin(\theta)\sin(\theta) = 1 - \cos(2\theta)$ and $2\cos(\theta)\sin(\theta) = \sin(2\theta)$, we get

$$u_{\mathrm{i}}(t) = x_{\mathrm{i}}(t) + x_{\mathrm{i}}(t)\cos(4\pi f_{\mathrm{c}}t) + x_{\mathrm{q}}(t)\sin(4\pi f_{\mathrm{c}}t), \tag{17}$$

$$u_{\mathrm{q}}(t) = x_{\mathrm{q}}(t) - x_{\mathrm{q}}(t)\cos(4\pi f_{\mathrm{c}}t) + x_{\mathrm{i}}(t)\sin(4\pi f_{\mathrm{c}}t). \tag{18}$$

After the high-frequency components of $u_{\mathrm{i}}(t)$ and $u_{\mathrm{q}}(t)$ are removed by the LPFs shown in Figure 12, we obtain

$$\hat{x}_{\mathrm{i}}(t) = x_{\mathrm{i}}(t), \tag{19}$$

$$\hat{x}_{\mathrm{q}}(t) = x_{\mathrm{q}}(t), \tag{20}$$

as desired.

Note that DSBSC can be thought of as a special case of QAM, in which $x_{\mathrm{q}}(t) = 0$.

1.4 Complex Quadrature Amplitude Modulation

Note that just like how the QAM scheme of Figure 12 transmits a signal comprising the two components $x_{\mathrm{i}}(t)$ and $x_{\mathrm{q}}(t)$, there are two components to a complex number, namely the real part and the imaginary part. Complex numbers can therefore conveniently represent the two parts of our signal, according to

$$x(t) = x_{\mathrm{i}}(t) + jx_{\mathrm{q}}(t), \tag{21}$$

where $j = \sqrt{-1}$.

Note that in a real circuit for a QAM modulator, we can't use an imaginary voltage to represent the quadrature-phase component $x_{\mathrm{q}}(t)$! Remember that complex numbers are *convenient*; they allow us to simplify the mathematics of complicated QAM schemes, while remaining equivalent to them, as we'll see below. Indeed, by using complex numbers, we can transform the (complicated) schematic of Figure 12 into the (simpler) one of Figure 13.

1.4.1 Mathematics

As shown in Figure 13

$$y(t) = \mathrm{Re}\left[x(t)\mathrm{e}^{-j2\pi f_{\mathrm{c}}t}\right], \tag{22}$$

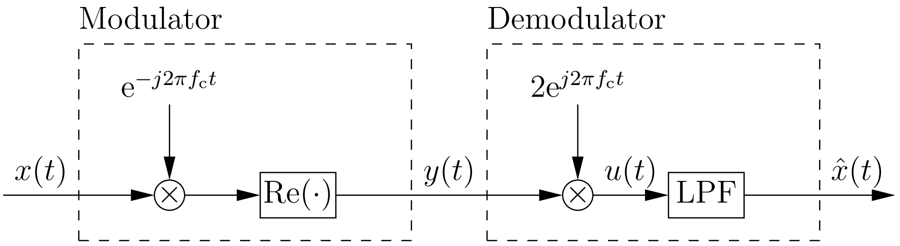

Figure 13: Complex QAM modulation and demodulation.

where $\mathrm{Re}[a + jb] = a$.

Using Euler's formula $e^{-j\theta} = \cos(\theta) - j\sin(\theta)$ and $j^2 = -1$, we get

$$\begin{aligned} y(t) &= \mathrm{Re}\left[x_\mathrm{i}(t)\cos(2\pi f_\mathrm{c} t) - jx_\mathrm{i}(t)\sin(2\pi f_\mathrm{c} t) + jx_\mathrm{q}(t)\cos(2\pi f_\mathrm{c} t) + x_\mathrm{q}(t)\sin(2\pi f_\mathrm{c} t)\right], \quad (23) \\ &= x_\mathrm{i}(t)\cos(2\pi f_\mathrm{c} t) + x_\mathrm{q}(t)\sin(2\pi f_\mathrm{c} t), \quad (24) \end{aligned}$$

just like in Equation 14. Hence, the approaches of Figures 12 and 13 are equivalent.

In the demodulator we have

$$u(t) = 2y(t)e^{j2\pi f_\mathrm{c} t}. \quad (25)$$

Using Euler's formula $e^{j\theta} = \cos(\theta) + j\sin(\theta)$ and the trigonometric product identities of Section 1.3, we get

$$\begin{aligned} u(t) = {} & 2x_\mathrm{i}(t)\cos(2\pi f_\mathrm{c} t)\cos(2\pi f_\mathrm{c} t) + 2x_\mathrm{q}(t)\sin(2\pi f_\mathrm{c} t)\cos(2\pi f_\mathrm{c} t) \\ & + j2x_\mathrm{q}(t)\sin(2\pi f_\mathrm{c} t)\sin(2\pi f_\mathrm{c} t) + j2x_\mathrm{i}(t)\cos(2\pi f_\mathrm{c} t)\sin(2\pi f_\mathrm{c} t), \quad (26) \\ = {} & x_\mathrm{i}(t) + x_\mathrm{i}(t)\cos(4\pi f_\mathrm{c} t) + x_\mathrm{q}(t)\sin(4\pi f_\mathrm{c} t) \\ & + jx_\mathrm{q}(t) - jx_\mathrm{q}(t)\cos(4\pi f_\mathrm{c} t) + jx_\mathrm{i}(t)\sin(4\pi f_\mathrm{c} t). \quad (27) \end{aligned}$$

After the high-frequency components of $u(t)$ are removed by the LPF shown in Figure 13, we obtain

$$\hat{x}(t) = x_\mathrm{i}(t) + jx_\mathrm{q}(t), \quad (28)$$

as desired.

1.4.2 Phasors

Note that the complex signal $x(t)$ can be represented using a phasor. Here,

$$x(t) = x_\mathrm{i}(t) + jx_\mathrm{q}(t) = |x(t)|e^{j\angle x(t)}, \quad (29)$$

where the amplitude $|x(t)|$ and phase $\angle x(t)$ are given by

$$|x(t)| = \sqrt{x_\mathrm{i}^2(t) + x_\mathrm{q}^2(t)}, \quad (30)$$

$$\angle x(t) = \arctan(x_\mathrm{q}(t)/x_\mathrm{i}(t)). \quad (31)$$

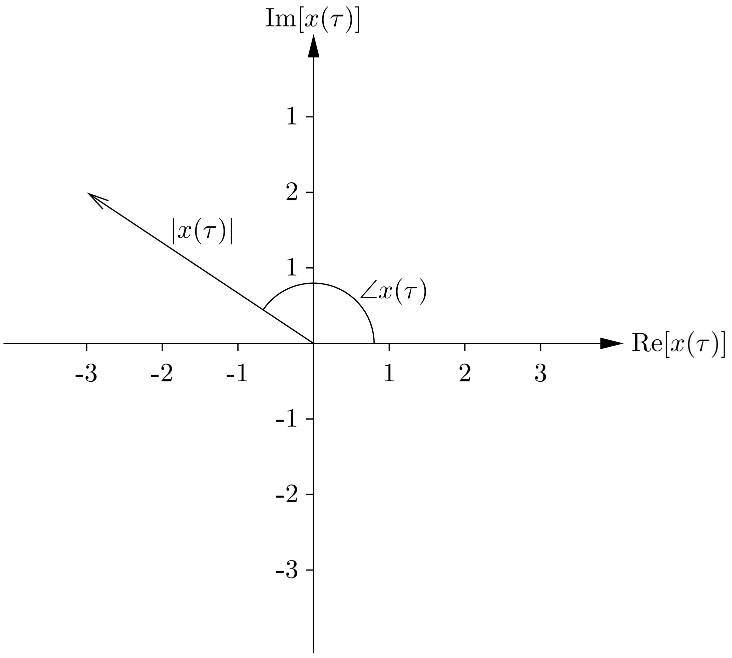

Figure 14: Phasor diagram for a complex signal $x(\tau) = -3 + 2j$.

For example, suppose that at a particular time instant where $t = \tau$, the signal has a value of $x(\tau) = -3 + 2j$. In this case $|x(\tau)| = \sqrt{13}$ and $\angle x(\tau) = 2.55$ radians, as shown in the *phasor diagram* of Figure 14.

Note that 'amplitude and phase' can have a number of slightly different meanings when considering the phasors of sinusoidal signals, like the modulated carrier $y(t)$ in Figures 9, 12 and 13. This is because a sinusoid $c(t) = A\cos(2\pi ft + \theta)$ will always have a purely real value, irrespective of which time instant τ we pick for t. Hence, if we were to draw $c(\tau) = A\cos(2\pi f\tau + \theta)$ in a phasor diagram, we would always get a phase of $\angle c(\tau) = 0$, while the amplitude $|c(\tau)| = A\cos(2\pi f\tau + \theta)$ would depend on the particular value of τ and therefore be time varying. However, $A\cos(2\pi ft + \theta) = \mathrm{Re}[Ae^{j(2\pi ft+\theta)}] = \mathrm{Re}[Ae^{j2\pi ft}e^{j\theta}]$. Therefore, phasor diagrams are sometimes drawn for $c'(\tau) = Ae^{j(2\pi f\tau+\theta)}$, where $c(t) = \mathrm{Re}[c'(t)]$. Here, the phase $\angle c'(\tau) = 2\pi f\tau + \theta$ is time varying, while the amplitude $|c'(\tau)| = A$ is constant. However, most frequently, phasor diagrams are drawn for $c'' = Ae^{j\theta}$, where $c(t) = \mathrm{Re}[c''e^{j2\pi ft}]$. In this case, both the phase $\angle c'' = \theta$ and the amplitude $|c''| = A$ are constant. Here, the phasor diagram is typically annotated with the sinusoid's frequency f, which is its third parameter.

1.5 Carrier recovery

As described in Section 1.2, the receiver is required to determine the frequency and phase of the carrier before it can perform coherent detection, as employed in DSBSC and QAM schemes. This process is called *carrier recovery* and it enables the receiver to generate the signal $2e^{j2\pi f_c t}$, as shown in Figure 13.

However, in the case where carrier recovery fails, the receiver will generate the signal $2e^{j(2\pi[f_c+f_\delta]t+\theta_\delta)} = 2e^{j(2\pi f_c t+\beta)}$ instead, where f_δ is the frequency error, θ_δ is the phase error and $\beta = 2\pi f_\delta t + \theta_\delta$.

In this case, it can be shown that the signal recovered by the scheme of Figure 13 will be

$$\hat{x}(t) = x_{\mathrm{i}}(t)\cos(\beta) - x_{\mathrm{q}}(t)\sin(\beta) + jx_{\mathrm{q}}(t)\cos(\beta) + jx_{\mathrm{i}}(t)\sin(\beta). \tag{32}$$

By comparing Equations 21 and 32, we can see that phase and frequency errors cause the real part of $\hat{x}(t)$ to become contaminated by $x_{\mathrm{q}}(t)$. Likewise, the imaginary part of $\hat{x}(t)$ becomes contaminated by $x_{\mathrm{i}}(t)$. In other words, the two signals $x_{\mathrm{i}}(t)$ and $x_{\mathrm{q}}(t)$ will interfere with each other.

In fact, in cases where there is a $\pi/2$ phase error and no frequency error, we obtain $\beta = \theta_\delta = \pi/2$ and

$$\hat{x}(t) = -x_{\mathrm{q}}(t) + jx_{\mathrm{i}}(t). \tag{33}$$

In this case, the signals $x_{\mathrm{i}}(t)$ and $x_{\mathrm{q}}(t)$ have swapped with each other!

Furthermore, in cases where there is a frequency error f_δ, the real and imaginary parts of $\hat{x}(t)$ will resemble QAM signals. For example, when there is no phase error we obtain $\beta = 2\pi f_\delta t$ and

$$\mathrm{Re}[\hat{x}(t)] = x_{\mathrm{i}}(t)\cos(2\pi f_\delta t) - x_{\mathrm{q}}(t)\sin(2\pi f_\delta t), \tag{34}$$

which is similar to Equation 14. As a result, the recovered message signals will be shifted in the frequency domain from the baseband to become centered at f_δ.

These results show that owing to their coherent nature, it is vital for DSBSC and QAM schemes to successfully perform carrier recovery.

1.6 Channels with additive complex noise

So far, we've assumed that our channel does not adversely affect our transmitted signal $y(t)$. Let's see how our analogue modulation scheme performs when the channel imposes time-varying additive complex noise $n(t) = n_{\mathrm{i}}(t) + jn_{\mathrm{q}}(t)$. This may be used to simulate Additive White Gaussian Noise (AWGN) by using a Gaussian distribution to randomly select uncorrelated values for the real $n_{\mathrm{i}}(t)$ and imaginary $n_{\mathrm{q}}(t)$ parts of $n(t)$.

A channel having additive complex noise is shown in Figure 15.

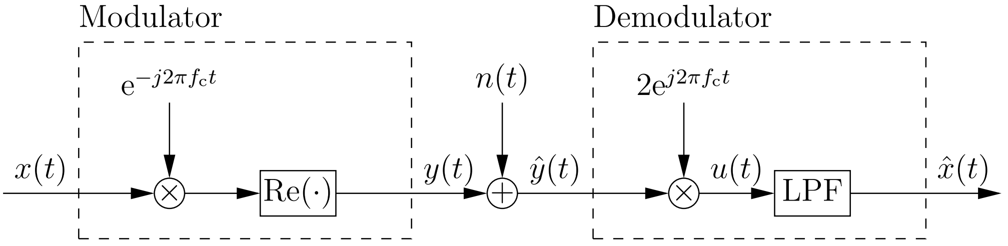

Figure 15: Complex QAM modulation and demodulation when the channel has additive complex noise.

1.6.1 Mathematics

In this case, we have

$$\hat{y}(t) = y(t) + n(t), \tag{35}$$

$$u(t) = 2\hat{y}(t)e^{j2\pi f_c t} \tag{36}$$

$$= 2y(t)e^{j2\pi f_c t} + 2n(t)e^{j2\pi f_c t}. \tag{37}$$

Using Euler's formula $\mathrm{e}^{j\theta} = \cos(\theta) + j\sin(\theta)$ and the result for $2y(t)e^{j2\pi f_c t}$ from Equation 27, we obtain

$$\begin{aligned} u(t) = {} & x_\mathrm{i}(t) + x_\mathrm{i}(t)\cos(4\pi f_\mathrm{c} t) + x_\mathrm{q}(t)\sin(4\pi f_\mathrm{c} t) \\ & + jx_\mathrm{q}(t) - jx_\mathrm{q}(t)\cos(4\pi f_\mathrm{c} t) + jx_\mathrm{i}(t)\sin(4\pi f_\mathrm{c} t) \\ & + 2n_\mathrm{i}(t)\cos(2\pi f_\mathrm{c} t) - 2n_\mathrm{q}(t)\sin(2\pi f_\mathrm{c} t) \\ & + j2n_\mathrm{q}(t)\cos(2\pi f_\mathrm{c} t) + j2n_\mathrm{i}(t)\sin(2\pi f_\mathrm{c} t). \end{aligned} \tag{38}$$

At first glance it seems as if the LPF of Figure 15 will remove the various components of the noise $n(t)$, since they has been shifted up to the carrier frequency by the multiplication with $2e^{j2\pi f_c t}$. However, if the noise is *white* (like AWGN) then it will affect all frequencies. As a result, the noise will still affect the base band, even after the shift. Hence, the LPF of Figure 15 will only *filter* the noise, not remove it. The resultant recovered signal will therefore be

$$\hat{x}(t) = x_\mathrm{i}(t) + jx_\mathrm{q}(t) + n'_\mathrm{i}(t) + jn'_\mathrm{q}(t) \tag{39}$$

$$= x(t) + n'(t), \tag{40}$$

where $n'(t)$ is the shifted and filtered noise. This demonstrates that we can simply add the equivalent noise components $n'_\mathrm{i}(t)$ and $n'_\mathrm{q}(t)$ to the in-phase signal $x_\mathrm{i}(t)$ and the quadrature-phase signal $x_\mathrm{q}(t)$, rather than going the whole-hog and simulating their modulation onto the channel.

1.7 Channels with a complex gain

In addition to additive complex noise, a channel can impose a complex gain $a(t) = a_\mathrm{i}(t) + ja_\mathrm{q}(t)$ (which may vary with time). A complex channel gain can be used to simulate the path loss, slow fading and fast fading of narrowband channels. In the case of path loss, a purely-real value (i.e. $a_\mathrm{q}(t) = 0$) that does not vary with time is typically selected for $a(t)$ using the Hata model. A purely-real constant value is also used in the case of slow fading. However, in this case, the value of $a(t)$ is randomly selected from a lognormal distribution. In order to evaluate the effect of this selection, we typically run a number of simulations, using a different randomly selected value for $a(t)$ in each. The performance observed in the various simulations can then be averaged to get an overall performance metric. In the case of fast fading, complex time-varying values are used for $a(t)$. The real a_i and imaginary a_q parts of these values will be randomly selected using a Gaussian distribution, yielding magnitudes having a Rician or Rayleigh distribution. Furthermore, a Doppler filter may be applied to induce correlation. Of course, the product of the path loss, slow fading and fast fading channel gains can be used for $a(t)$, when simulating a channel exhibiting all of these characteristics.

A channel having a complex gain is shown in Figure 16.

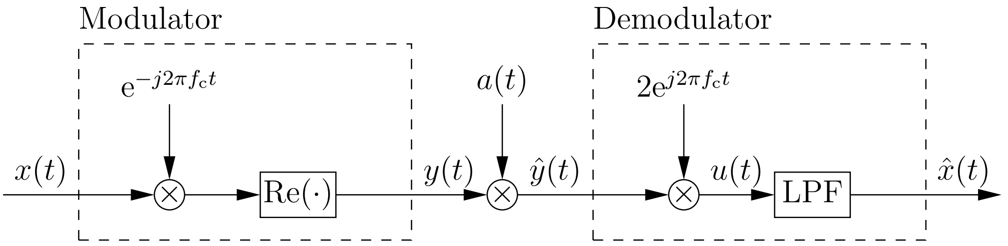

Figure 16: Complex QAM modulation and demodulation when the channel has a complex gain.

1.7.1 Mathematics

In this case, we have

$$\hat{y}(t) = a(t)y(t). \tag{41}$$

Using Equation 24, we obtain

$$\begin{aligned}\hat{y}(t) = {} & a_\mathrm{i}(t)x_\mathrm{i}(t)\cos(2\pi f_\mathrm{c}t) + a_\mathrm{i}(t)x_\mathrm{q}(t)\sin(2\pi f_\mathrm{c}t) \\ & + ja_\mathrm{q}(t)x_\mathrm{i}(t)\cos(2\pi f_\mathrm{c}t) + ja_\mathrm{q}(t)x_\mathrm{q}(t)\sin(2\pi f_\mathrm{c}t),\end{aligned} \tag{42}$$

Using Euler's formula $e^{j\theta} = \cos(\theta) + j\sin(\theta)$ and the trigonometric product identities of Section 1.3, we get

$$\begin{aligned}u(t) = {} & a_\mathrm{i}(t)x_\mathrm{i}(t) + a_\mathrm{i}(t)x_\mathrm{i}(t)\cos(4\pi f_\mathrm{c}t) + a_\mathrm{i}(t)x_\mathrm{q}(t)\sin(4\pi f_\mathrm{c}t) \\ & + ja_\mathrm{q}(t)x_\mathrm{i}(t) + ja_\mathrm{q}(t)x_\mathrm{i}(t)\cos(4\pi f_\mathrm{c}t) + ja_\mathrm{q}(t)x_\mathrm{q}(t)\sin(4\pi f_\mathrm{c}t) \\ & + ja_\mathrm{i}(t)x_\mathrm{q}(t) - ja_\mathrm{i}(t)x_\mathrm{q}(t)\cos(4\pi f_\mathrm{c}t) + ja_\mathrm{i}(t)x_\mathrm{i}(t)\sin(4\pi f_\mathrm{c}t) \\ & - a_\mathrm{q}(t)x_\mathrm{q}(t) + a_\mathrm{q}(t)x_\mathrm{q}(t)\cos(4\pi f_\mathrm{c}t) - a_\mathrm{q}(t)x_\mathrm{i}(t)\sin(4\pi f_\mathrm{c}t).\end{aligned} \tag{43}$$

After the high-frequency components of $u(t)$ are removed by the LPF shown in Figure 16, we obtain

$$\begin{aligned}\hat{x}(t) &= a_\mathrm{i}(t)x_\mathrm{i}(t) + ja_\mathrm{q}(t)x_\mathrm{i}(t) + ja_\mathrm{i}(t)x_\mathrm{q}(t) - a_\mathrm{q}(t)x_\mathrm{q}(t), && (44)\\ &= (a_\mathrm{i}(t) + ja_\mathrm{q}(t))(x_\mathrm{i}(t) + jx_\mathrm{q}(t)), && (45)\\ &= a(t)x(t), && (46)\end{aligned}$$

which shows that the complex gain $a(t)$ can be applied directly to the complex signal $x(t)$, without simulating its modulation onto the channel!

The effect of the channel be evaluated by considering $a(t)$ and $x(t)$ as phasors. When two phasors are multiplied together, the result is a phasor having an amplitude equal to the product of the two original amplitudes, while the resultant phase is given by the sum of the original phases. Hence,

$$\begin{aligned}|\hat{x}(t)| &= |a(t)| \cdot |x(t)|, && (47)\\ \angle\hat{x}(t) &= \angle a(t) + \angle x(t). && (48)\end{aligned}$$

Therefore, the channel changes the amplitude and phase of the signal $x(t)$.

1.7.2 Equivalence

You may wonder how we can use complex numbers (which have an imaginary component) for a real-life thing like the gain of a channel. Well, a complex gain is a convenient way of representing a channel that changes the amplitude *and* the phase of the transmitted signal $y(t)$. Consider the case where the channel of Figure 12 (which does not use complex numbers) replaces $y(t)$ of Equation 14 with

$$\hat{y}(t) = |a(t)|x_{\mathrm{i}}(t)\cos(2\pi f_{\mathrm{c}}t - \angle a(t)) + |a(t)|x_{\mathrm{q}}(t)\sin(2\pi f_{\mathrm{c}}t - \angle a(t)), \tag{49}$$

where

$$|a(t)| = \sqrt{a_{\mathrm{i}}^2(t) + a_{\mathrm{q}}^2(t)}, \tag{50}$$

$$\angle a(t) = \arctan(a_{\mathrm{q}}(t)/a_{\mathrm{i}}(t)). \tag{51}$$

In this case, the scheme of Figure 12 would obtain the equivalent result to Equation 44, with

$$\hat{x}_{\mathrm{i}}(t) = a_{\mathrm{i}}(t)x_{\mathrm{i}}(t) - a_{\mathrm{q}}(t)x_{\mathrm{q}}(t), \tag{52}$$

which is the real part of Equation 44, as well as

$$\hat{x}_{\mathrm{q}}(t) = a_{\mathrm{i}}(t)x_{\mathrm{q}}(t) + a_{\mathrm{q}}(t)x_{\mathrm{i}}(t), \tag{53}$$

which is the imaginary part of Equation 44. The difference is that the mathematics would have been even more complicated!

Note that Equations 52 and 53 show that the effect of a channel having a complex gain is to cause $x_{\mathrm{i}}(t)$ and $x_{\mathrm{q}}(t)$ to interfere with eachother. This may be attributed to the phase difference $\angle a(t)$ between the received carrier and that generated locally in the receiver. Note that this is the same result as that obtained when carrier recovery fails, as described in Section 1.5. In fact, successful carrier recovery can detect and rectify the phase difference imposed by the channel. Therefore, we are typically most interested in the *magnitude* of the complex gain $|a(t)|$.

1.8 Channels with a complex gain and additive complex noise

Wireless channels typically impose a complex gain and additive complex noise. These channels can be modelled using the schematic of Figure 17.

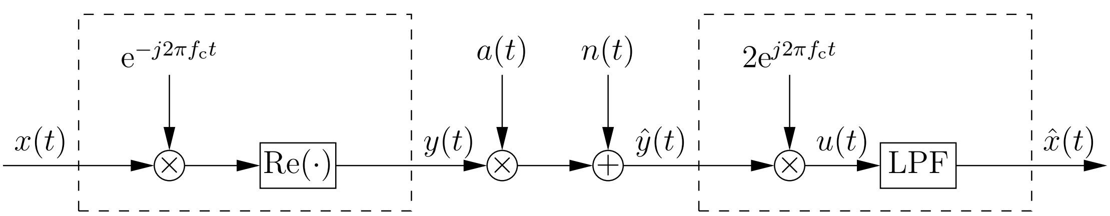

Figure 17: Complex QAM modulation and demodulation when the channel has a complex gain and additive complex noise.

As described in Section 1.7, carrier recovery techniques can be used to rectify the phase difference imposed by the channel's complex gain. Furthermore, amplification can be used to compensate for the magnitude of the complex gain. However, this will also amplify any additive complex noise, which cannot be easily mitigated. For this reason, noise is particularly detrimental in wireless channels.

2 Digital Modulation

2.1 16-ary Quadrature Amplitude Modulation

The previous section showed that analogue modulation schemes are susceptible to noise. In this section, we'll show that digital modulation schemes can achieve reliable communications even in the presence of relatively severe noise. The difference between an analogue and a digital modulation scheme is the type of signal they are used to convey. As we showed in Section 1, analogue modulators transmit an analogue signal $x(t)$. However, the analogue demodulator can never be sure if a particular component of the demodulated signal $\hat{x}(t)$ is signal or noise. By contrast, digital modulators transmit digital signals, such as a sequence of binary digits $b[n]$. Since a bit can only have a value of '0' or '1', the demodulator just has to choose from these two values when recovering the sequence $\hat{b}[n]$. While the demodulator can never be sure that it has made the right choices, it will typically do a good job so long as the noise is not really bad.

We can construct a digital modulation scheme by converting the digital signal $b[n]$ into an analogue signal $x(t)$ and using the analogue modulation scheme of Figure 15. Once the demodulated signal $\hat{x}(t)$ has been recovered, we just need to convert it back into a digital signal $\hat{b}[n]$. Schematics for a Digital to Analogue Converter (DAC) and an Analogue to Digital Converter (ADC) are provided in Figures 18 and 19.

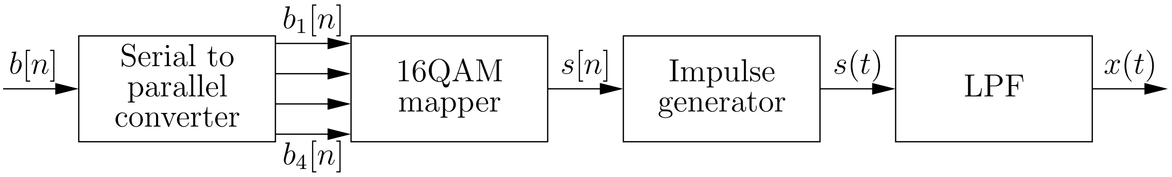

Figure 18: Digital to analogue conversion using 16QAM.

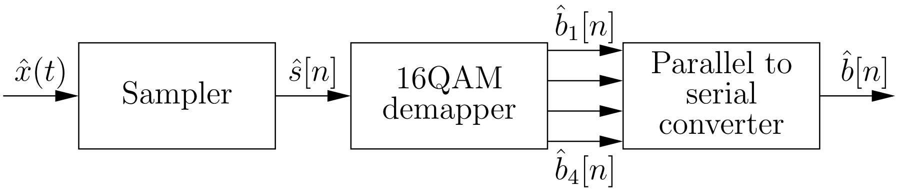

Figure 19: Analogue to digital conversion using 16QAM.

2.1.1 Serial to parallel conversion

Consider the case where we wish to convey the bit sequence $b[n]$ by sending $k = 4$ bits at a time. The first step is to convert our serial sequence of bits $b[n]$ into four parallel sequences

$b_1[n]$, $b_2[n]$, $b_3[n]$ and $b_4[n]$, as shown in Figure 18. This is achieved by decomposing $b[n]$ into groups of four bits and distributing these among the four bit sequences $b_1[n]$, $b_2[n]$, $b_3[n]$ and $b_4[n]$. For example, suppose that

$$\{b[n]\}_{n=1}^{20} = [0,0,1,1,1,0,1,1,0,0,1,1,0,0,0,0,1,1,1,1]. \tag{54}$$

This gives

$$\begin{aligned}
\{b_1[n]\}_{n=1}^{5} &= [b[1], b[5], b[9], b[13], b[17]] = [0,1,0,0,1], && (55)\\
\{b_2[n]\}_{n=1}^{5} &= [b[2], b[6], b[10], b[14], b[18]] = [0,0,0,0,1], && (56)\\
\{b_3[n]\}_{n=1}^{5} &= [b[3], b[7], b[11], b[15], b[19]] = [1,1,1,0,1], && (57)\\
\{b_4[n]\}_{n=1}^{5} &= [b[4], b[8], b[12], b[16], b[20]] = [1,1,1,0,1]. && (58)
\end{aligned}$$

2.1.2 Bit mapping

The $M = 16$-ary Quadrature Amplitude Modulation (16QAM) bit mapper of Figure 18 converts the four bit sequences $b_1[n]$, $b_2[n]$, $b_3[n]$ and $b_4[n]$ into a single sequence of *symbols* $s[n]$. Since there are $M = 2^k = 16$ possible combinations of $k = 4$ bits, we require $M = 16$ different values for the symbols of $s[n]$. Note that these values can be complex, since this is supported by the modulator of Figure 15. We can therefore visualise the $M = 16$ different symbol values as phasors in a *constellation diagram.* Figure 20 provides the 16QAM constellation diagram, in which $M = 16$ constellation points are arranged in a 4×4 grid.

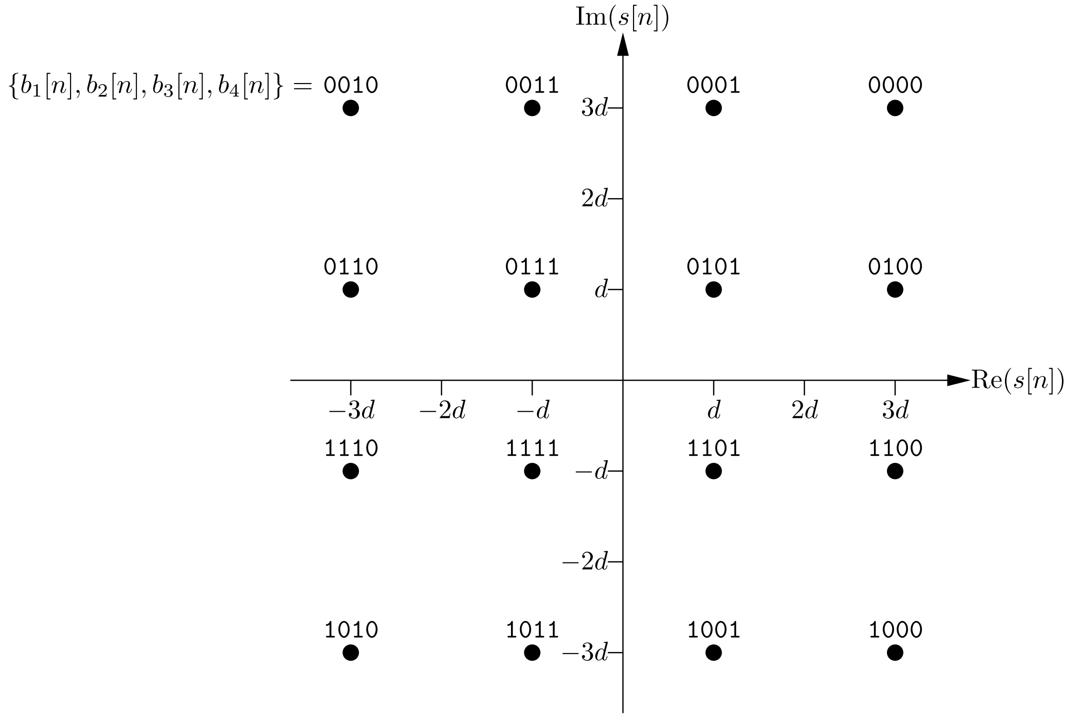

Figure 20: 16QAM constellation diagram showing the Gray bit mapping.

As shown in Figure 20, each of the $M = 16$ different combinations of the four bits is *mapped* to a different one of the $M = 16$ constellation points. Here, *Gray bit mapping* is employed, which ensures that the bit combinations that are mapped to neighbouring constellation points differ only by one bit. The number of bits that differ in a pair of bit combinations is called their *Hamming distance.*

As shown in Figure 20, neighbouring constellation points are separated by a *Euclidean distance* of $2d$. The value chosen for d affects the average transmit power. As shown in Figure 20, when $\{b_1[n], b_2[n], b_3[n], b_4[n]\}$ has a value of `0101`, `0111`, `1111` or `1101`, $|s[n]| = \sqrt{d^2 + d^2}$ according to the Pythagorean theorem. By contrast, if $\{b_1[n], b_2[n], b_3[n], b_4[n]\}$ has a value of `0100`, `0001`, `0011`, `0110`, `1110`, `1011`, `1001` or `1100`, then $|s[n]| = \sqrt{(3d)^2 + d^2}$. Finally, `0000`, `0010`, `1010` and `1000` result in $|s[n]| = \sqrt{(3d)^2 + (3d)^2}$. If we assume that all constellation points occur equally likely, then the average transmit power is given by $E\{|s[n]|^2\} = 4/16 \cdot 2d^2 + 8/16 \cdot 10d^2 + 4/16 \cdot 18d^2 = 10d^2$. If we want this to be unity, we can employ $d = \sqrt{1/10}$.

For the example $b_1[n]$, $b_2[n]$, $b_3[n]$ and $b_4[n]$ bit sequences of Equations 55 – 58,

$$\{s[n]\}_{n=1}^{5} = [-d + 3dj, -d - 3dj, -d + 3dj, 3d + 3dj, -d - dj]. \tag{59}$$

2.1.3 Impulse generation

As shown in Figure 18, the next step is to convert our sequence of discrete 16QAM symbols $s[n]$ into a continuous function of time $s(t)$. Suppose that we want to transmit our symbol sequence $s[n]$ at a rate of $f_{\text{symbol}} = 10000$ symbols per second. Each symbol therefore has a period of $t_{\text{symbol}} = 1/f_{\text{symbol}} = 0.1$ ms. We can obtain a continuous function of time $s(t)$ by generating impulses having the corresponding complex amplitudes in the middle of each symbol period. Figure 21 shows this for the example $s[n]$ of Equation 59.

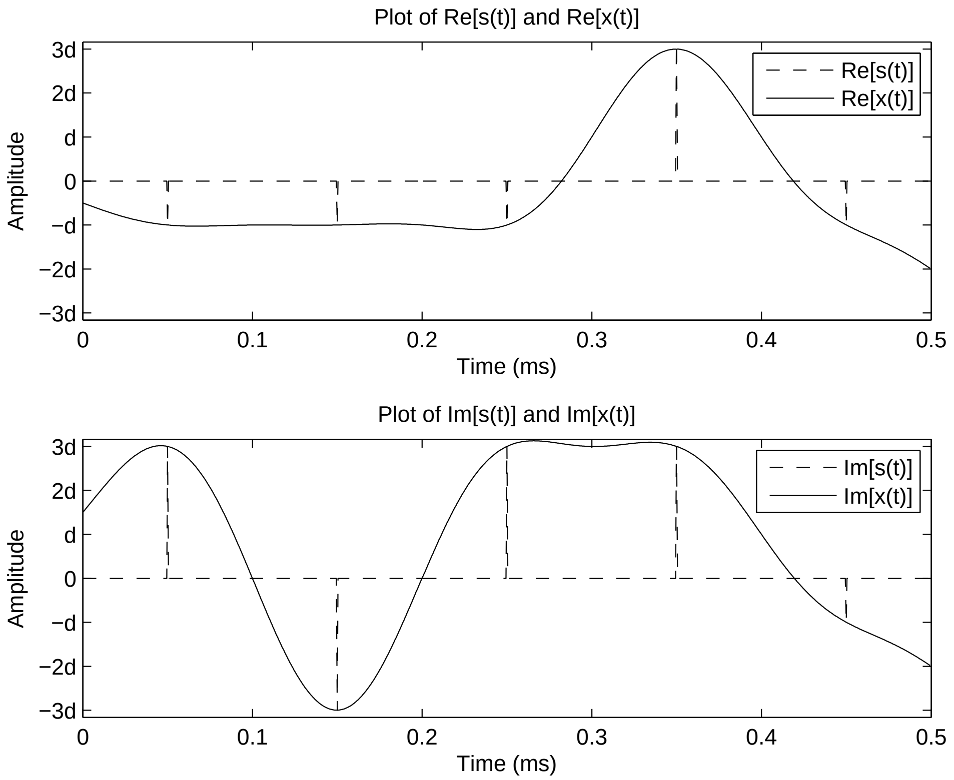

Figure 21: Plots of the real and imaginary parts of the signals $s(t)$ and $x(t)$ that corresponds to the example $s[n]$ of Equation 59. Here, $x(t)$ has been obtained by using the raised cosine filter characterised in Figure 22 to shape the pulses of $s(t)$.

2.1.4 Pulse shaping

As exemplified in Figure 21, the signal $s(t)$ changes very rapidly. As a result, the maximum frequency $f_{\max}$ in $s(t)$ is very high. If we were to modulate $s(t)$ on to the channel, then a very high bandwidth B would result, since $B = 2f_{\max}$, as described in Section 1.2.2. For this reason, we must apply a special type of LPF called a *Nyquist filter* to $s(t)$ before transmitting it, as shown in Figure 18. The frequency response of an example Nyquist filter is provided in Figure 22. This frequency response resembles half of a cosine cycle, that has been raised so that it is above the horizontal axis. For this reason, this LPF is called a *raised cosine filter*.

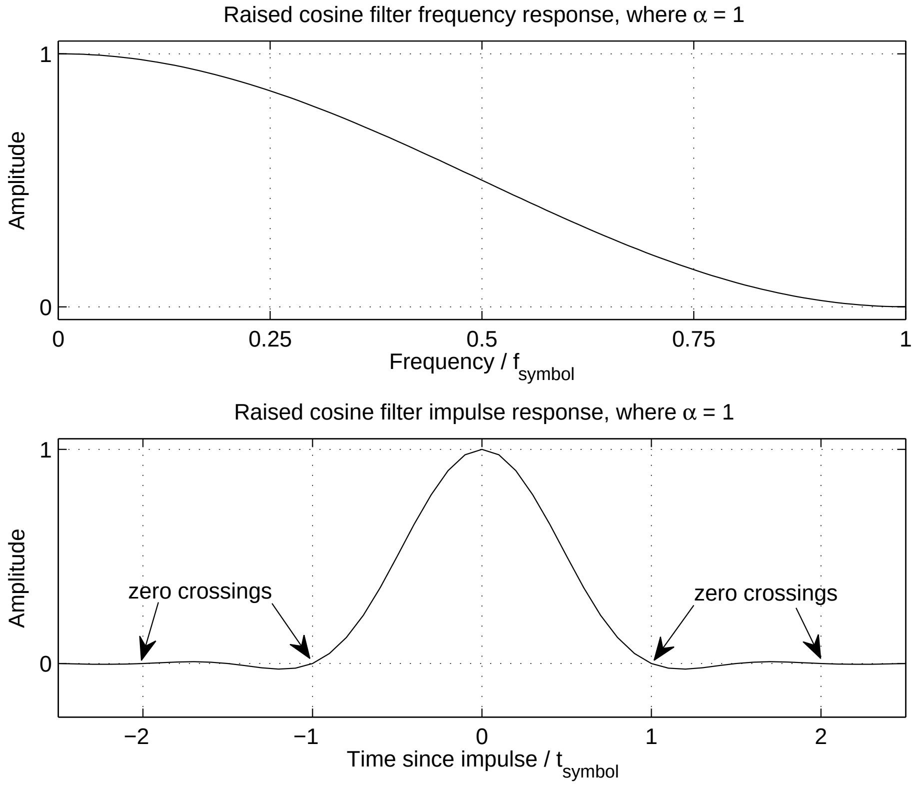

Figure 22: Plots of the impulse and frequency response of a raised cosine filter having a roll-off factor of $\alpha = 1.0$.

The LPF of Figure 18 is referred to as a *pulse shaping filter*, since it reshapes the impulses of $s(t)$ so that they do not comprise any high frequency components. The manner in which the pulse shaping filter reshapes the impulses of $s(t)$ is characterised by its *impulse response*. In addition to the frequency response of a pulse shaping filter, Figure 22 also provides the corresponding impulse response. In the scheme of Figure 18, the signal $x(t)$ is obtained by *convolving* the signal $s(t)$ with the pulse shaping filter's impulse response. This replaces each impulse in the signal $s(t)$ with a version of the pulse shaping filter's impulse response having the same amplitude and position in time. The signal $x(t)$ is obtained by summing all of the time-shifted impulse responses together at each moment in time. Figure 21 exemplifies this for the case of using the raised cosine filter characterised in Figure 22.

Observe in Figure 21 that $x(t) = s(t)$ whenever $s(t)$ is impulsed. This may seem surprising, since each point on $x(t)$ is obtained by summing together all of the time-shifted impulse responses, as described above. However, the impulse responses of raised cosine filters have *zero crossings* whenever the time since the impulse is a non-zero integer multiple of the symbol period t_{symbol}, as shown in Figure 22. As a result, the value of $x(t)$ at an instant when $s(t)$ is impulsed is affected only by the corresponding impulse response; all of the other time-shifted impulse responses will be zero at this moment. This special feature of raised cosine filters means that they avoid *Inter-Symbol Interference* (ISI).

In general, raised cosine filters have cut-off frequencies equal to half the symbol rate f_{symbol}. They are parameterised by their *roll-off factor* $0 \leq \alpha \leq 1$, which determines the steepness of their frequency response The raised cosine filter that is characterised in Figure 22 employs the maximal value for its roll-off factor of $\alpha = 1$. As a result, the amplitude of its frequency response gradually changes from 1 to 0. This frequency response is called the *full-cosine roll-off characteristic.*

A steeper frequency response is exemplified in Figure 23, in which $\alpha = 0.5$. In general, the amplitude of a raised cosine filter's frequency response is unity for frequencies between 0 and $(1-\alpha)f_{\text{symbol}}/2$, as shown in Figure 23. Furthermore, the frequency response resembles a raised cosine between frequencies of $(1-\alpha)f_{\text{symbol}}/2$ and $(1+\alpha)f_{\text{symbol}}/2$. Note that the *transition bandwidth* is given by $(1+\alpha)f_{\text{symbol}}/2 - (1-\alpha)f_{\text{symbol}}/2 = \alpha f_{\text{symbol}}$. Finally, for frequencies above

$$f_{\max} = (1+\alpha)f_{\text{symbol}}/2, \tag{60}$$

the amplitude of a raised cosine filter's frequency response is zero, as shown in Figure 23. Here, $f_{\max}$ is the highest frequency that will not be totally filtered out in $x(t)$. Note that $f_{\max} = 10$ kHz in the example $x(t)$ of Figure 21, since $f_{\text{symbol}} = 10$ kHz and $\alpha = 1$ in this case.

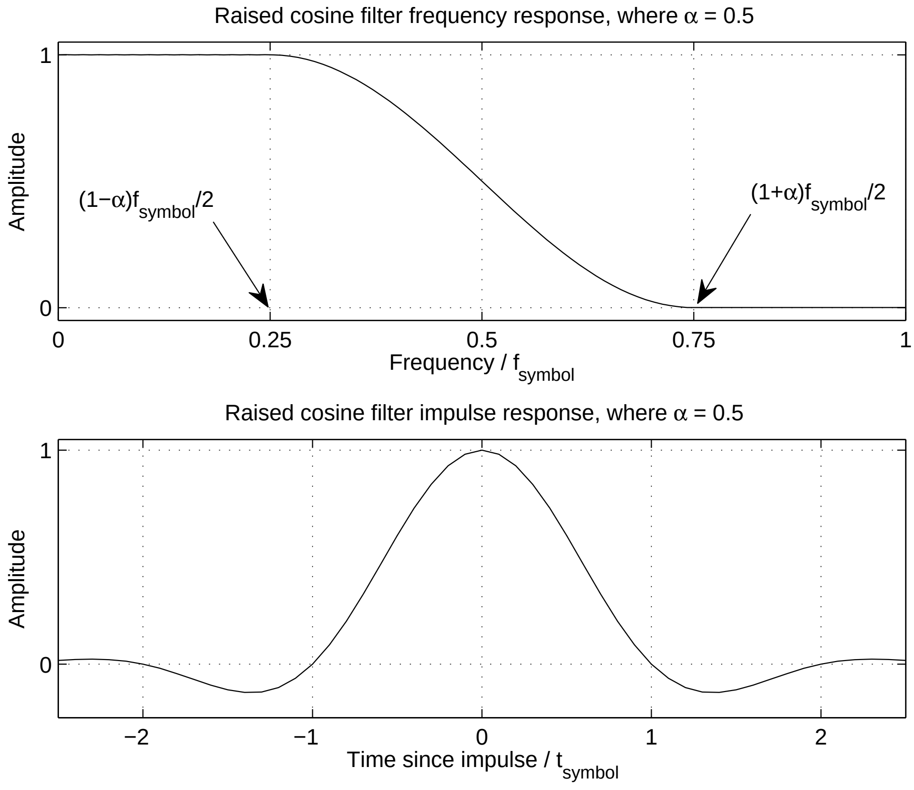

Figure 23: Plots of the impulse and frequency response of a raised cosine filter having a roll-off factor of $\alpha = 0.5$.

When the minimal value of $\alpha = 0$ is employed for the roll-off factor, an *ideal Nyquist filter* results. As shown in Figure 24, an ideal Nyquist filter has a brickwall frequency response. Note that Figure 24 also provides the corresponding impulse response, which may be obtained using the sinc function according to $\mathrm{sinc}(t/t_{\mathrm{symbol}})$, where $\mathrm{sinc}(x) = \sin(\pi x)/(\pi x)$.

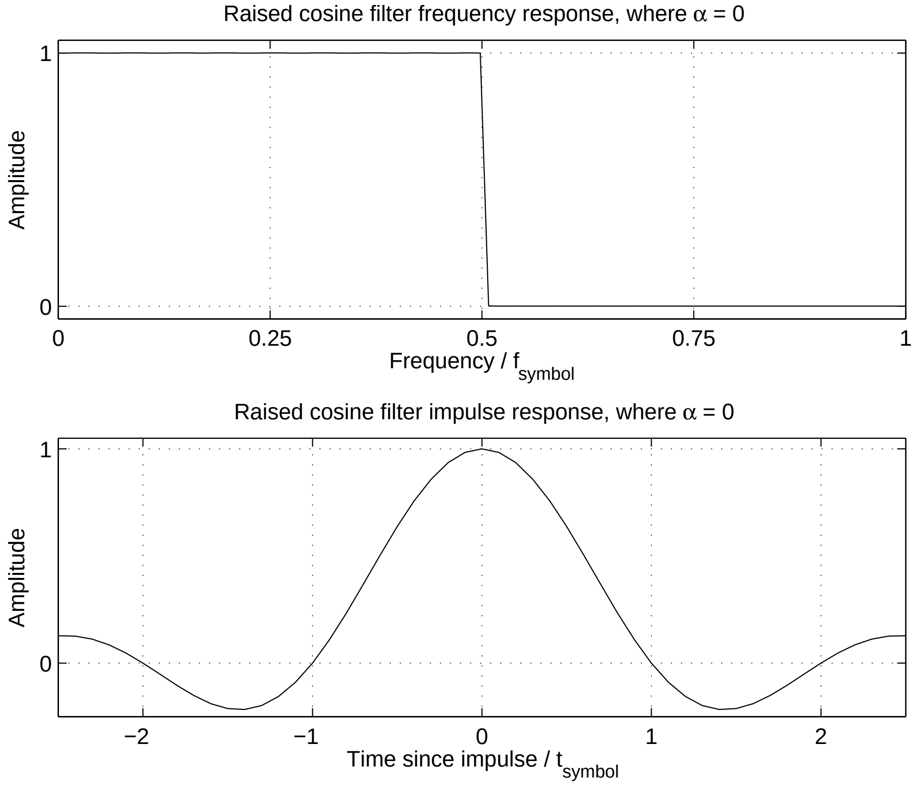

Figure 24: Plots of the impulse and frequency response of an ideal Nyquist filter, which has a roll-off factor of $\alpha = 0$.

According to Equation 13, the bandwidth B of an AM signal is double the maximum frequency f_{max} present in the signal $x(t)$. When a raised cosine filter is employed for pulse shaping, f_{max} is given by Equation 60. Hence, the bandwidth required may be obtained by combining Equations 13 and 60, yielding

$$B = (1 + \alpha) f_{\mathrm{symbol}}. \tag{61}$$

Therefore, low values of the roll-off factor α have the benefit of reducing the amount of bandwidth required B.

However, Figures 22 – 24 show that low roll-off factors are associated with impulse responses that take longer to decay towards zero. As a result, impractically high orders are required in order to implement raised cosine filters having low roll-off factors. Furthermore, when low roll-off factors are employed, the receiver is much more sensitive to offsets in its synchronisation with the transmitter.

2.1.5 Matched filters

Suppose that the scheme of Figure 15 was employed to transmit the signal $x(t)$ of Figure 21 over a severe AWGN channel. Also suppose that the LPF of Figure 15 employed a cut-off frequency of 250 kHz. In this case, the reconstructed signal $\hat{x}(t)$ that is provided to the ADC of Figure 19 would look nothing like the transmitted signal $x(t)$, as exemplified in Figure 25. As described in Section 2.1.4, the signal $x(t)$ comprises components having frequencies of up to $f_{\mathrm{max}} = 10$ kHz.

However, the PSD of Figure 25 shows that the reconstructed signal $\hat{x}(t)$ comprises components having frequencies of up to 250 kHz, which is the cut-off frequency employed for the LPF of Figure 15. These components may be attributed to unfiltered AWGN. Clearly, some of the noise in the reconstructed signal $\hat{x}(t)$ could be removed by using a lower cut-off frequency for the LPF of Figure 15. However, if this cut-off frequency is reduced too far, then some of the desired signal $x(t)$ may be filtered away too.

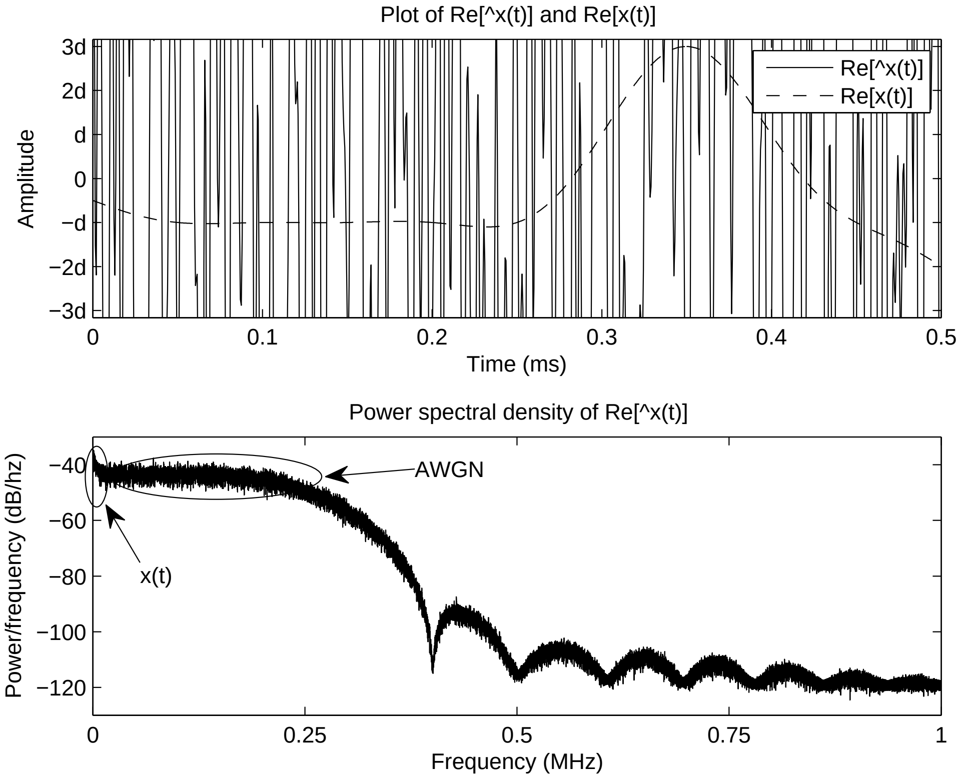

Figure 25: Plot and PSD of the real part of the modulated signal $\hat{x}(t)$ from Figure 19 when matched filters are not employed.

The solution is to use *matched filters* in the transmitter and receiver. More specifically, if the LPFs of Figures 18 and 15 have the same design, then a maximum amount of AWGN can be removed, without filtering the desired signal away. The combination of the transmit and receive filters has a frequency response given by the product of their individual responses. We want this overall frequency response to be a raised cosine so that ISI can be avoided, as described in Section 2.1.4. Therefore we should employ filters having frequency responses that are the *square root* of the raised cosine response. These filters are therefore called *root raised cosine filters.*

Returning to our example, consider the case where the transmit and receive filters are replaced with root raised cosine filters having roll-off factors of $\alpha = 1$. Using the same AWGN as in the example of Figure 25 in this case results in the reconstructed signal $\hat{x}(t)$ shown Figure 26. Note that this much more closely resembles the transmitted signal $x(t)$, demonstrating the benefit of matched filters.

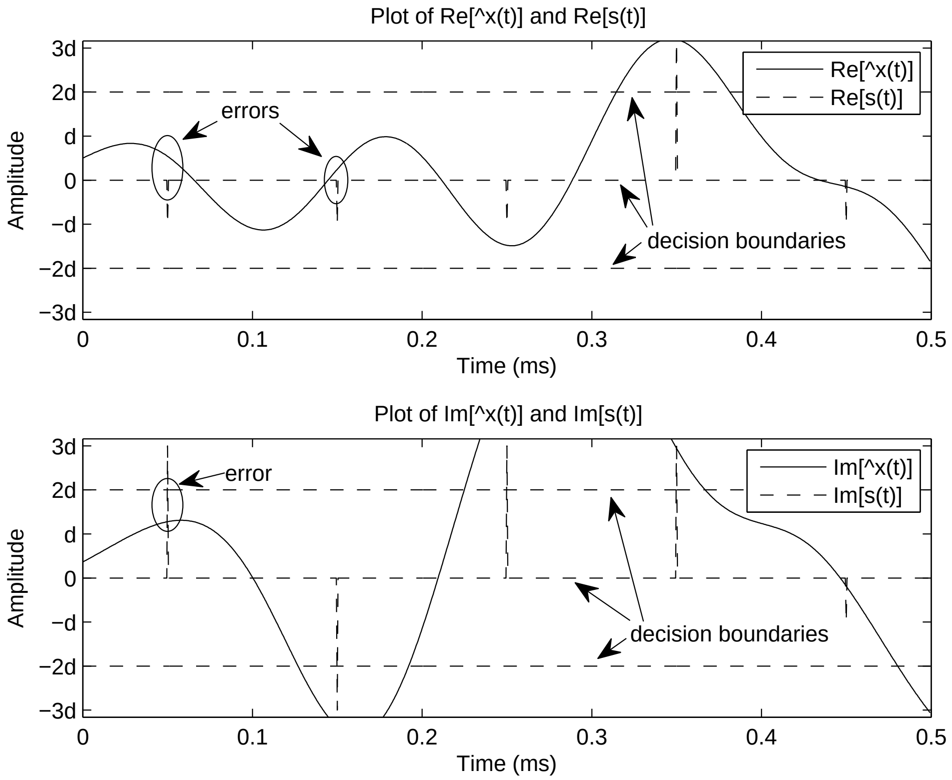

Figure 26: Plot of the real and imaginary parts of the modulated signal $\hat{x}(t)$ from Figure 19 when matched filters are employed.

2.1.6 Decisions, decisions, decisions

It is the job of the ADC shown in Figure 19 to consider the reconstructed signal $\hat{x}(t)$ and decide which bit values to output for $b[n]$. The first step is to sample $\hat{x}(t)$ at the time instances where the signal $s(t)$ was impulsed in the transmitter. To help illustrate this, Figure 26 includes plots of the real and imaginary parts of both $\hat{x}(t)$ and $s(t)$. The resultant samples $\hat{s}[n]$ are then obtained, as shown in Figure 19. For the example signal $\hat{x}(t)$ of Figure 26, we get

$$\{\hat{s}[n]\}_{n=1}^{5} = [0.079 + 0.487j, 0.016 - 1.052j, -0.445 + 1.451j, 0.999 + 0.928j, -0.092 - 0.104j]. \tag{62}$$

These phasors are plotted in the 16QAM constellation diagram of Figure 27. The corresponding values for the bit sequences $\hat{b}_1[n]$, $\hat{b}_2[n]$, $\hat{b}_3[n]$ and $\hat{b}_4[n]$ are obtained by selecting the constellation point that is nearest to each phasor. Figure 27 includes dashed lines that identify the regions in which each constellation point is the nearest. Note that these *decision boundaries* are located at $-2d$, 0 and $2d$ on both the real and imaginary axes. The corresponding decision boundaries are included in the plot of $\hat{x}(t)$ in Figure 26.

In the case of the samples of Equation 62, we obtain the reconstructed bit sequences

$$\{\hat{b}_1[n]\}_{n=1}^{5} = [0, 1, 0, 0, 1], \tag{63}$$

$$\{\hat{b}_2[n]\}_{n=1}^{5} = [1, 0, 0, 0, 1], \tag{64}$$

$$\{\hat{b}_3[n]\}_{n=1}^{5} = [0, 0, 1, 0, 1], \tag{65}$$

$$\{\hat{b}_4[n]\}_{n=1}^{5} = [1, 1, 1, 0, 1]. \tag{66}$$

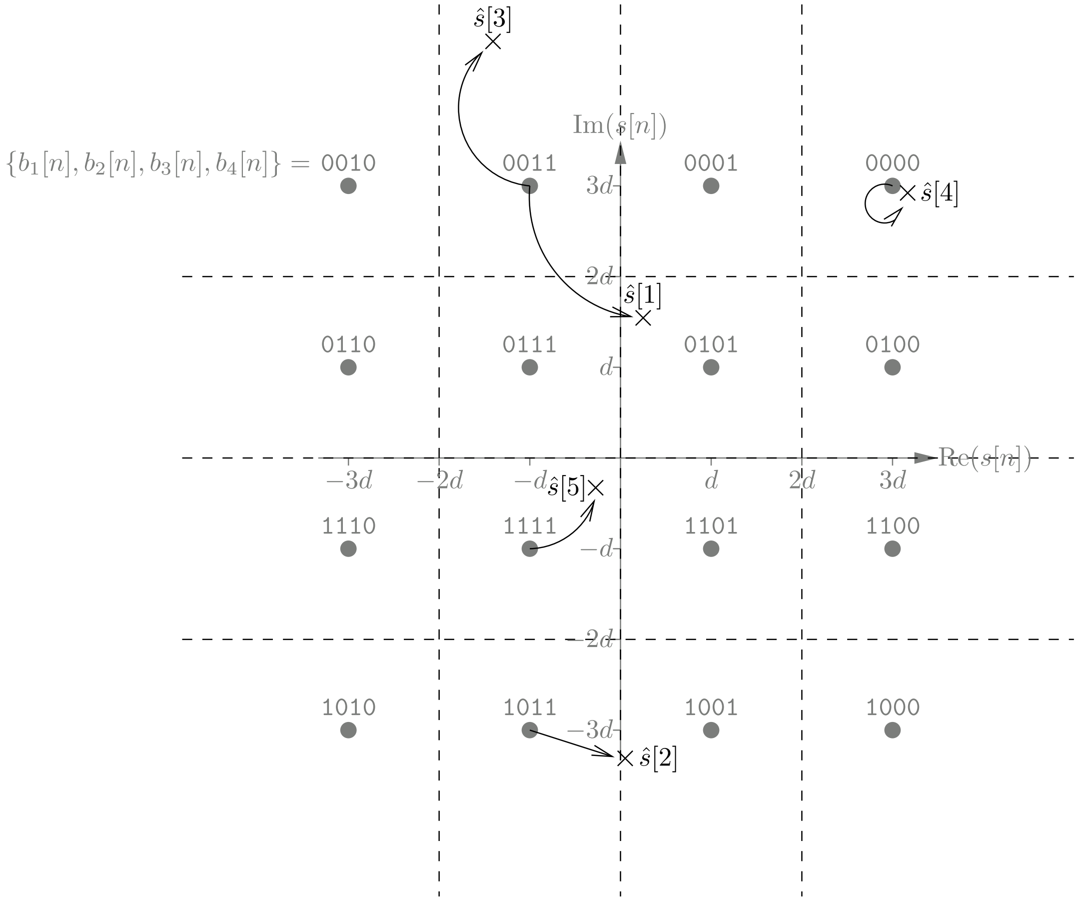

Figure 27: 16QAM constellation diagram showing the positions of the reconstructed symbols $\hat{s}[n]$ of Equation 62.

By comparing these bit sequences with those of Equations 55 – 58 we can see that three bit errors have occurred. These may be attributed to the positioning of the samples in $\hat{s}[n]$ within the wrong regions of Figure 27. Note that two bit errors have occurred, owing to the incorrect positioning of the sample $\hat{s}[1]$, while $\hat{s}[2]$ has caused only one bit error. This is because the noise has displaced $\hat{s}[1]$ further than $\hat{s}[2]$.

As described in Section 2.1.2, the Gray bit mapping of Figure 20 results in a Hamming distance of one between each pair of constellation points that are separated by the minimum Euclidean distance of $2a$. Since AWGN channels are most likely to displace the samples of $\hat{s}[n]$ by a small Euclidean distance, Gray bit mapping results in a minimal BER.

Note that $\hat{b}_2[n]$ and $\hat{b}_4[n]$ are more susceptible to bit errors than $\hat{b}_1[n]$ and $\hat{b}_3[n]$. As shown in Figure 28, this is because every constellation point has a Euclidean distance of d from the nearest decision boundary for $\hat{b}_2[n]$ and $\hat{b}_4[n]$. By contrast, some of the constellation points have a Euclidean distance of $3d$ from the decision boundary for $\hat{b}_1[n]$ and $\hat{b}_3[n]$. Therefore, more noise is required to corrupt these bits.

Finally, the reconstructed bit sequence $\hat{b}[n]$ is obtained by performing the parallel to serial conversion of the sequences $\hat{b}_1[n]$, $\hat{b}_2[n]$, $\hat{b}_3[n]$ and $\hat{b}_4[n]$. In the case of the sequences of Equations 63 – 66, we obtain the 20-bit sequence

$$\{\hat{b}[n]\}_{n=1}^{20} = [0, 1, 0, 1, 1, 0, 0, 1, 0, 0, 1, 1, 0, 0, 0, 0, 1, 1, 1, 1], \tag{67}$$

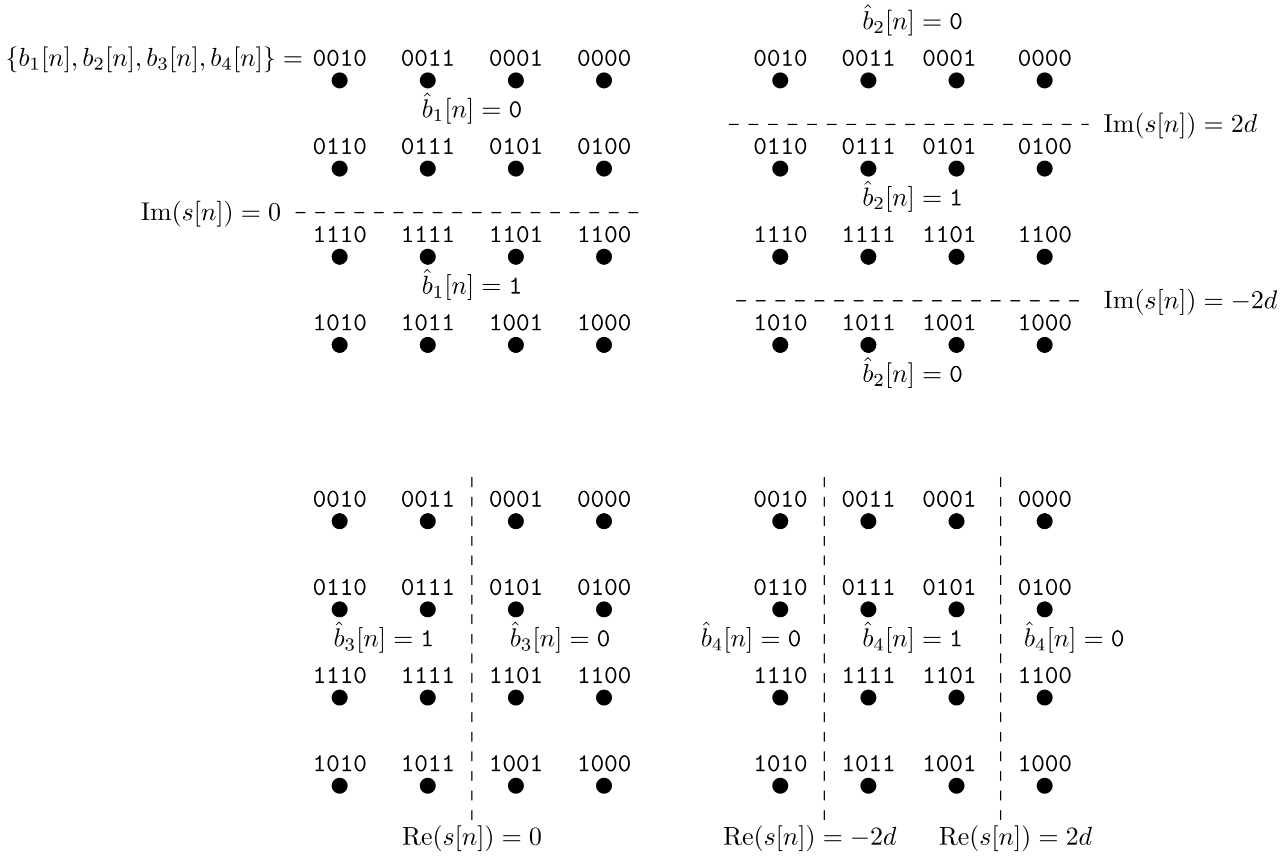

Figure 28: Decision boundaries for Gray bit mapped 16QAM.

which contains three bit errors, as described above. This corresponds to a *Bit Error Ratio* (BER) of $3/20 = 0.15$.

2.1.7 Eye diagrams

In the previous section, the presence of noise in the channel caused a high BER to result. This effect can be analysed by considering the corresponding *eye diagram*. Before we do this however, it is useful to draw an eye diagram for the case where there is no noise in the channel, for the sake of allowing a comparison. This eye diagram is shown in Figure 29.

The eye diagram of Figure 29 was obtained by first decomposing the signal $\hat{x}(t)$ into segments having durations equal to the symbol period $t_{\text{symbol}} = 0.1$ ms. Following this, the real and imaginary part of each pair of consecutive segments was plotted in Figure 29. The resultant figure is referred to as an eye diagram because it comprises empty regions that are shaped like eyes.

Note that in order for these eye-shaped regions to appear, the signal $\hat{x}(t)$ must be long. For this reason, the 0.5 ms signal $\hat{x}(t)$ that was used in the previous sections was extended to have a duration of 10.1 ms before the eye diagram of Figure 29 was drawn. Here, a duration of 10.1 ms can be decomposed into 101 segments having durations of $t_{\text{symbol}} = 0.1$ ms. Hence, there are 100 possible pairings of consecutive segments and Figure 29 contains 100 plots.

Observe that at the time instants labelled 0.05 ms and 0.15 ms in Figure 29, there are only

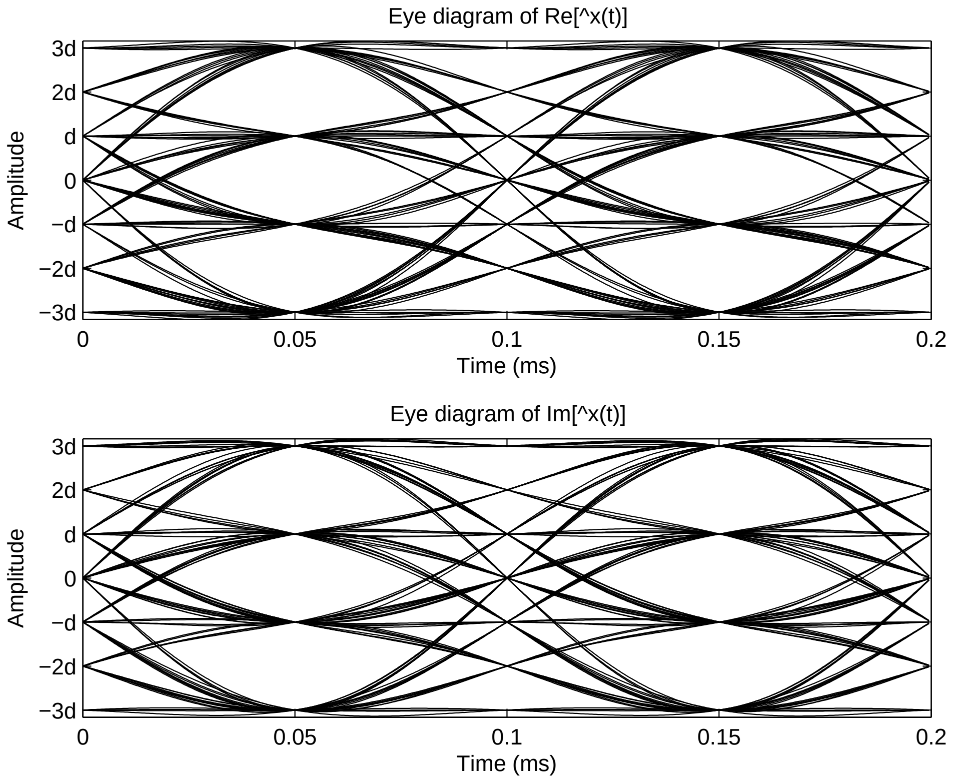

Figure 29: Eye diagram for 16QAM using a roll-off factor of $\alpha = 1$ in the case where there is no noise in the channel.

four possible amplitudes for the real and imaginary parts of $\hat{x}(t)$, namely $-3d$, $-d$, d and $3d$. This is because these time instants correspond to the middles of the consecutive symbol periods represented in Figure 29. At these time instants, $\hat{x}(t)$ has a value equal to the corresponding symbol in $s[n]$ when there is no noise in the channel, as described in the previous sections. Since the real and imaginary parts of $s[n]$ can only take values of $-3d$, $-d$, d and $3d$ in 16QAM, these are the only amplitudes that are possible for the real and imaginary parts of $\hat{x}(t)$ at the time instants labelled 0.05 ms and 0.15 ms in Figure 29.

Between the time instants labelled 0.05 ms and 0.15 ms in Figure 29, the real and imaginary parts of $\hat{x}(t)$ can be seen to take sixteen different paths, depending on the value of the two corresponding consecutive symbols in $s[n]$. Note that the paths have a non-zero width. This is because the path that $\hat{x}(t)$ takes between two particular values of two corresponding consecutive symbols in $s[n]$ also depends on the values of previous and subsequent symbols in $s[n]$, owing to the tails in the impulse response of the pulse shaping filters, as described in Section 2.1.4. As shown in Figure 30, this effect is exaggerated if the roll-off factor of the root raised cosine filters is reduced from $\alpha = 1$ to $\alpha = 0.5$, since this results in an impulse response having longer tails.

The ‘open-ness’ of the eye-shaped regions in the eye diagram show how easy it is for the 16QAM demapper to make the correct decisions. If the eyes are closed, then it is difficult for the demapper to make the correct decisions, particularly if the sampler of Figure 19 is not perfectly synchronised with the impulse generator of Figure 18. For this reason, the BER is more sensitive to the synchronisation if a lower roll-off factor α is used, as described in Section 2.1.5. This is the cost of using a lower bandwidth.

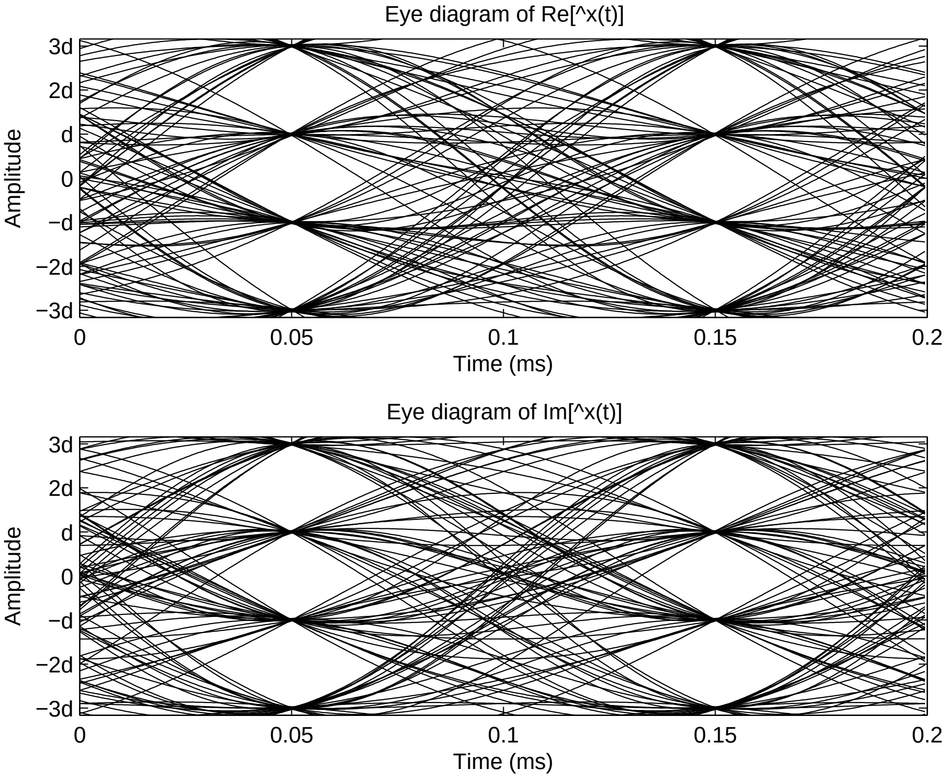

Figure 30: Eye diagram for 16QAM using a roll-off factor of $\alpha = 0.5$ in the case where there is no noise in the channel.

Returning to a roll-off factor of $\alpha = 1$, the eye diagram of Figure 31 shows the effect of introducing a moderate amount of noise in the channel. Here, the eyes remain relatively open and a low BER could be expected. By contrast, Figure 32 provides an eye diagram for the case where the severe noise of Section 2.1.5 is introduced by the channel. The closed eyes shown in Figure 32 explain the high BER that was observed in Section 2.1.6.

2.2 Other digital modulation schemes

In Section 2.1 we considered 16QAM, which transmits $k = 4$ bits at a time by mapping each of the $M = 2^k = 16$ possible combinations of bits to a different constellation point, in the particular manner shown in Figure 20. However in general, any number k of bits can be sent at once. Furthermore, any mapping of the $M = 2^k$ different combinations to the $M = 2^k$ constellation points can be used. Finally, the $M = 2^k$ constellation points can be positioned anywhere in the complex plane. Of course, different modulation schemes are associated with different BER performances.

Schematics for a general DAC and ADC are provided in Figures 33 and 34. Note that these are the same as those of Figures 18 and 19, with the exception that k can take any integer value.

The differences between various digital modulation schemes are made readily apparent when their constellation diagrams are compared. Figures 35, 36 and 37 provide constellation diagrams for Binary ($M = 2$) Phase Shift Keying (BPSK), Quarternary ($M = 4$) Phase Shift Keying (QPSK) and $M = 8$-ary Phase Shift Keying (8PSK), respectively.

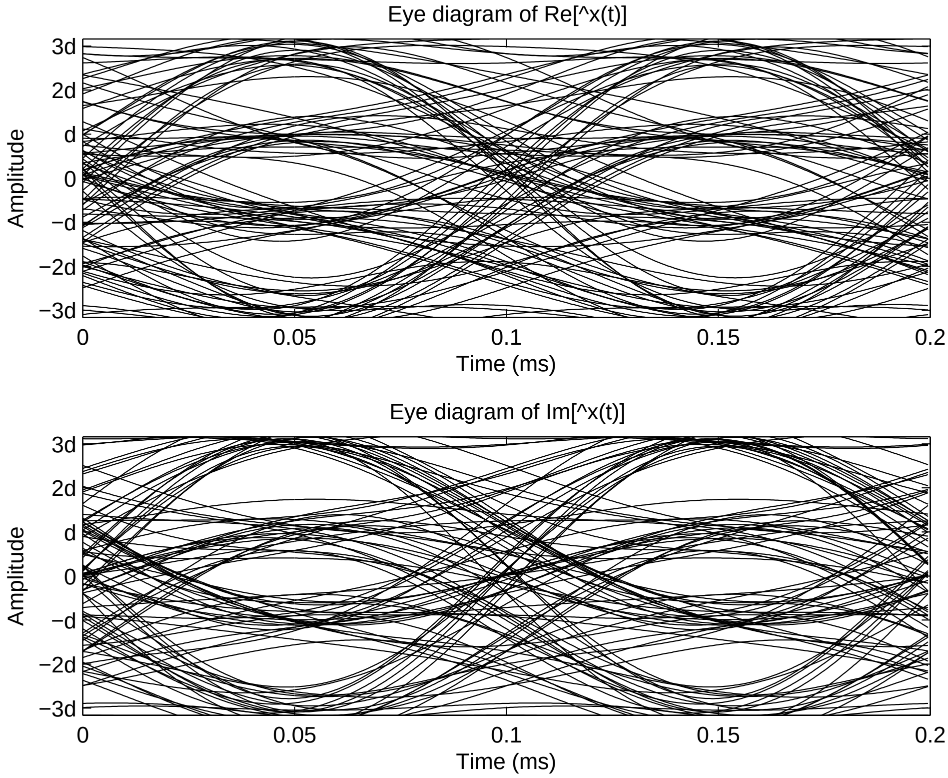

Figure 31: Eye diagram for 16QAM using a roll-off factor of $\alpha = 1$ in the case where there is moderate noise in the channel.

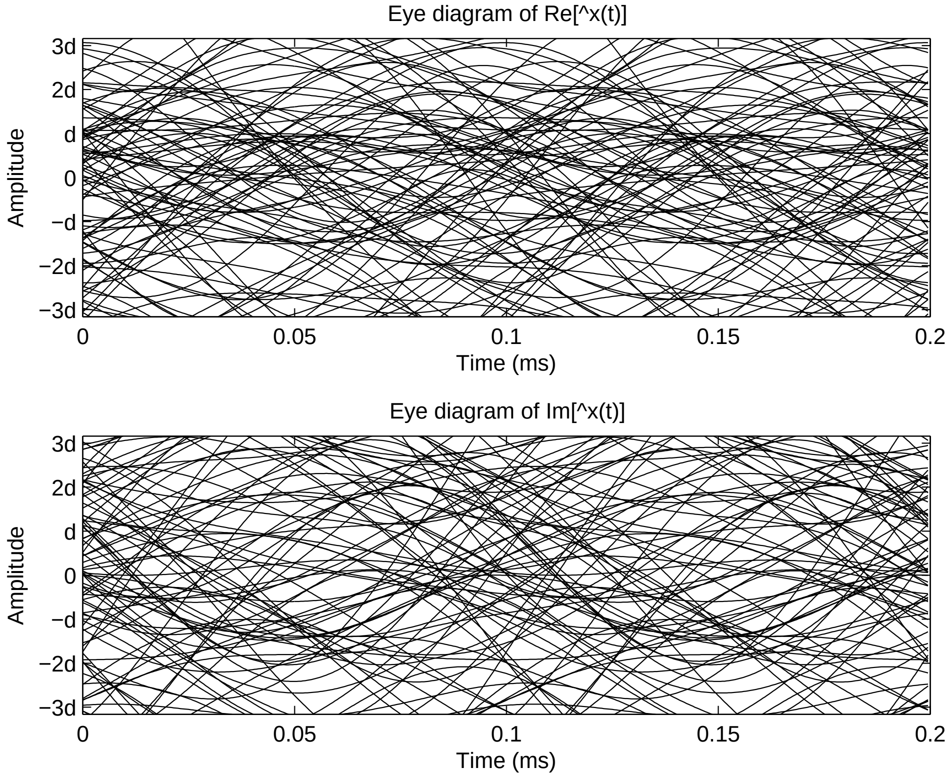

Figure 32: Eye diagram for 16QAM using a roll-off factor of $\alpha = 1$ in the case where there is severe noise in the channel.

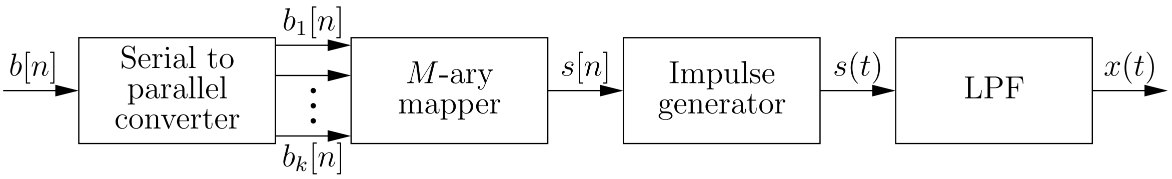

Figure 33: Digital to analogue conversion using M-ary modulation.

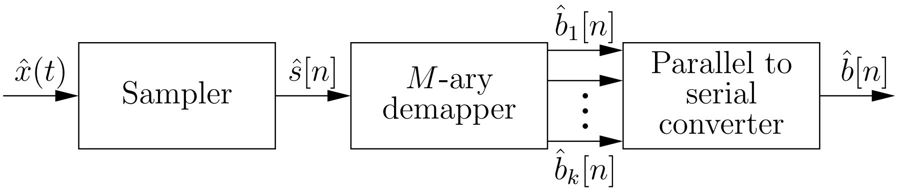

Figure 34: Analogue to digital conversion using M-ary modulation.

In these constellation diagrams, the various constellation points have the same amplitude, but different phases. It is for this reason that they are referred to as *phase* shift keying schemes. This is in contrast to the 16QAM constellation diagram of Figure 20, in which the constellation points are distinguished by their different real and imaginary amplitudes.

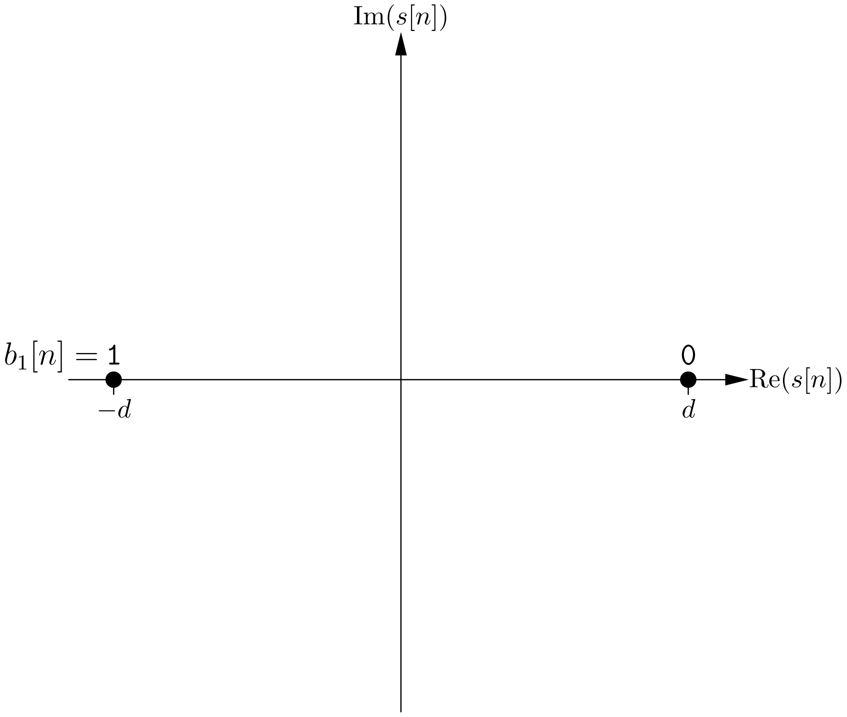

Figure 35: BPSK constellation diagram.

Note that the QPSK and 8PSK schemes employ Gray mapping. In other words, the bit combinations that are mapped to neighbouring constellation points have Hamming distances of one, like in the 16QAM constellation diagram shown in Figure 20. As a result, the BER is minimised, as described in Section 2.1.6.

Recall that $d = \sqrt{1/10}$ is required to normalise the average transmit power of the 16QAM scheme to unity, as described in Section 2.1.2. In order to normalise the transmit powers to unity, $d = 1$ is required for the BPSK and 8PSK schemes, since their transmit power is given

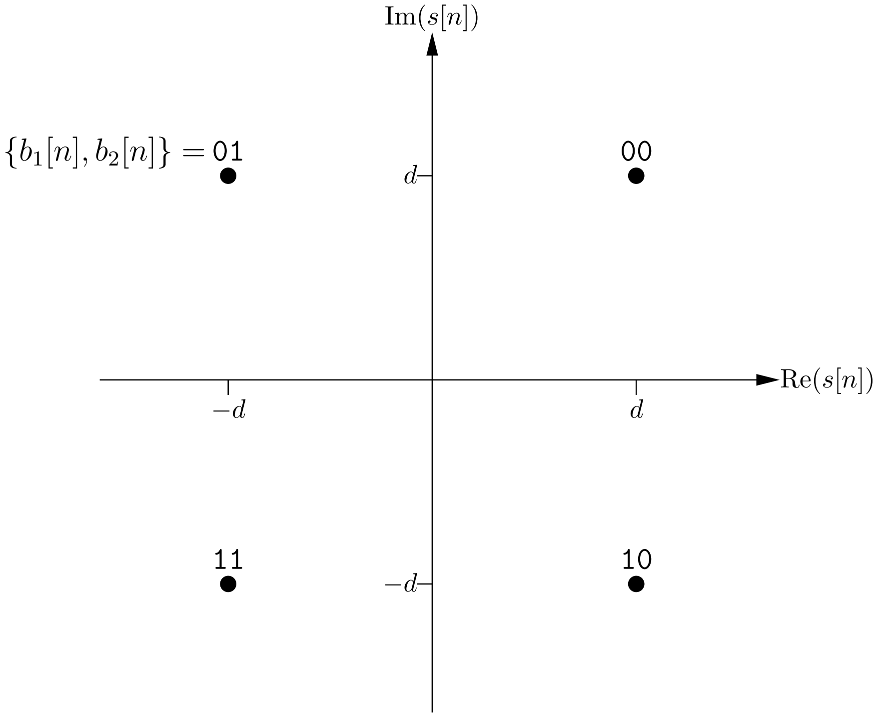

Figure 36: QPSK constellation diagram showing the Gray bit mapping.

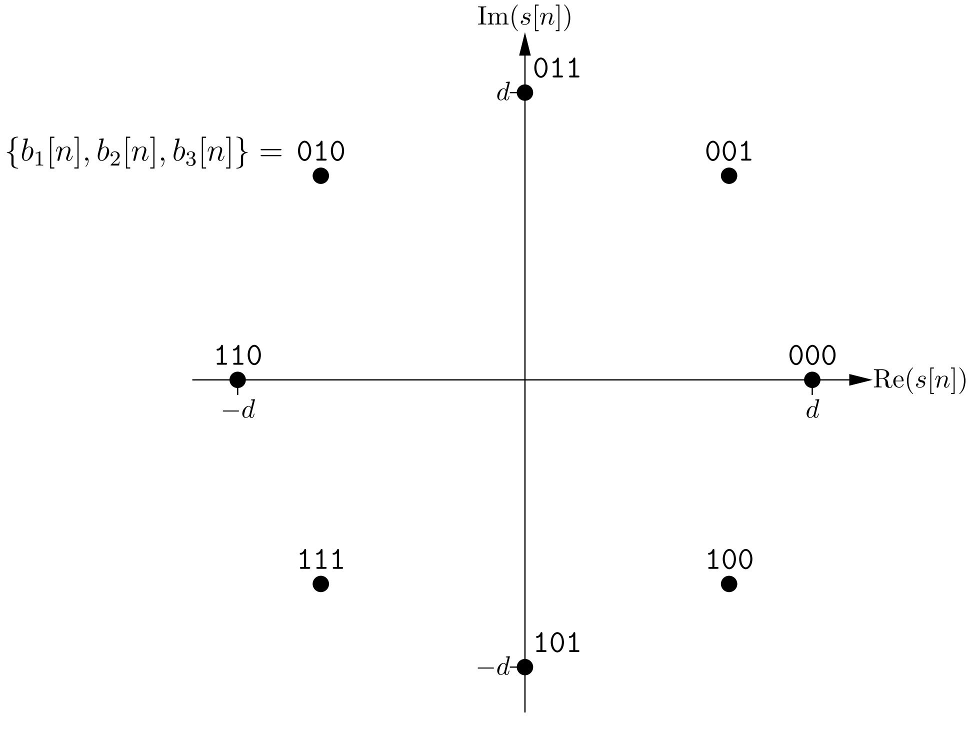

Figure 37: 8PSK constellation diagram showing the Gray bit mapping.

by $|s[n]| = d^2$. By contrast, the average transmit power is given by $|s[n]| = \sqrt{d^2 + d^2}$ in the QPSK scheme. As a result, $d = \sqrt{1/2}$ is required to normalise the transmit power to unity in this case.

While the operation of the serial to parallel converter and the M-ary mapper in Figure 33 depends on the choice of modulation scheme, the operation of the impulse generator and LPF is identical to in the 16QAM scheme described in Section 2.1. Likewise, the operation of the sampler shown in Figure 34 is identical to that described in Section 2.1.

Like the 16QAM demapper described in Section 2.1.6, the M-ary demapper of Figure 34 is tasked with determining which constellation point is the nearest to each reconstructed phasor in $\hat{s}[n]$. Note that as in the 16QAM scheme, the decision boundaries of the BPSK and QPSK schemes are parallel to either the real or imaginary axis. By contrast, the decision boundaries of the 8PSK scheme radiate from the centre of Figure 37, passing half-way between each pair of neighbouring constellation points.